The origin of early-mid Miocene pelagic brown and green claystone from IODP Site U1503A in the South China Sea: implications to paleoclimate and paleoceanography

Zhe Zhang[1] and Zhen Sun[1]

[1]CAS Key Laboratory of Ocean and Marginal Sea Geology, South China Sea Institute of Oceanology

November 23, 2022

Abstract

The marine pelagic brown claystone was widely recovered in the deep South China Sea (SCS) by International Ocean Discovery Program (IODP) Expedition 349, 367, 368 and 368X. The continuous deposition of brown claystone in Miocene in the SCS may represent a special sedimentary environment. IODP Site U1503A provides the ideal brown and green claystone of the early-mid Miocene to study the origin of the red coloring for sediments and their implications to the paleoclimate and paleoceanography. In this paper, the reflectance a*, grain size, clay minerals, major and trace elements, and Sr-Nd isotope analyses in brown and green claystone from U1503A have been conducted to understand the sedimentary condition and controlling factors of SCS marine brown claystone. The results show that the sediments color transition was caused by the variations of Fe (III) content. The provenance was relatively stable and sediment was mainly supplied from South China and Luzon. The source areas underwent strong chemical and physical weathering since 17 Ma, which is related to Miocene Climatic Optimum events. The data of redox proxies suggest that both brown and green claystone were deposited in the oxic condition, while the sedimentary environment of brown claystone was more oxidizing. We suggest this difference in the redox condition was mainly controlled by the variation of the oxygen-rich bottom current in the northern SCS. We attribute this variation to the larger-scale deep-water circulation change in the Antarctic and western Pacific due to glacial-deglacial cycle.

The origin of early-mid Miocene pelagic brown and green claystone from IODP Site U1503A in the South China Sea: implications to paleoclimate and paleoceanography

Zhe Zhang[1,2] Zhen Sun[1,2,3*]

[1] Southern Marine Science and Engineering Guangdong Laboratory (Guangzhou), Key Laboratory of Ocean and Marginal Sea Geology, South China Sea Institute of Oceanology, Innovation Academy of South China Sea Ecology and Environmental Engineering, Chinese Academy of Sciences, Guangzhou 511458, China

[2] University of Chinese Academy of Sciences, Beijing 100049, China

[3] China-Pakistan Joint Research Center on Earth Sciences, CAS-HEC, Islamabad 45320, Pakistan

[*] Corresponding author. Z. Sun, E-mail address: zhensun@scsio.ac.cn

Key points

1. High content of Fe (III) caused the brown color of early-mid Miocene sediment at Site U1503A.

2. The sediment color variation reflected redox condition change which was controlled by the strength of oxygen-rich bottom current in the SCS.

3. The ventilation and deep water current in the SCS were strongly affected by Pacific deep water circulation during the early-mid Miocene.

Abstract

The marine pelagic brown claystone was widely recovered in the deep South China Sea (SCS) by International Ocean Discovery Program (IODP) Expedition 349, 367, 368 and 368X. The continuous deposition of brown claystone in Miocene in the SCS may represent a special sedimentary environment. IODP Site U1503A provides the ideal brown and green claystone of the early-mid Miocene to study the origin of the red coloring for sediments and their implications to the paleoclimate and paleoceanography. In this paper, the reflectance a*, grain size, clay minerals, major and trace elements, and Sr-Nd isotope analyses in brown and green claystone from U1503A have been conducted to understand the sedimentary condition and controlling factors of SCS marine brown claystone. The results show that the sediments color transition was caused by the variations of Fe (III) content. The provenance was relatively stable and sediment was mainly supplied from South China and Luzon. The source areas underwent strong chemical and physical weathering since 17 Ma, which is related to Miocene Climatic Optimum events. The data of redox proxies suggest that both brown and green claystone were deposited in the oxic condition, while the sedimentary environment of brown claystone was more oxidizing. We suggest this difference in the redox condition was mainly controlled by the variation of the oxygen-rich bottom current in the northern SCS. We attribute this variation to the larger-scale deep-water circulation change in the Antarctic and western Pacific due to glacial-deglacial cycle.

Plain language summary

Marine pelagic brown or red sediment is of great significance to indicate the paleoclimate and deep-sea sedimentary condition because of its special color. International Ocean Discovery

Program (IODP) Expeditions 349, 367, 368 and 368X recovered pelagic brown claystone in sea basin of South China Sea (SCS). In order to understand the origin of the sediment color and its indications of the paleoclimate and paleo-ocean environment, we analyzed the composition of clay mineral, geochemical elements and grain size of the SCS brown and green claystone. The results show that the brown color is due to the high content of Fe (III) oxides (hematite or goethite). After excluding the effects of iron-bacterial mediation, sediment source, and erosion intensity, we inferred that the high content of Fe (III) may reflect oxic sedimentary conditions which was controlled by the strength of oxygen-rich bottom current in the SCS basin. The conclusions are important to understand the regional ventilation and deep water current changes under the glacial-deglacial cycle during the Miocene.

Keywords

IODP Site U1503A; the early-mid Miocene; marine brown and green claystone; South China Sea; redox conditions; deep water current

1. Introduction

Pelagic brown (dark reddish) claystone is widely discovered in the deep sea areas, especially on oceanic crust (Lyes, 1983; Hu et al., 2012a; Song et al., 2017). There have been long term discussions upon its origin (Löwemark et al., 2008; Hu et al., 2012a; Jin et al., 2020). Considering the spectacular reddish color, scientists try to decipher its origin through mineral, geochemistry and coloring process analysis.

The color of the sediment is generally believed to be caused by the Fe- or Mn-bearing minerals

(Lyes, 1983; Löwemark et al., 2008; Cai et al., 2009; Hu et al., 2012a). For example, Lyles (1983) suggested that the brown-tan-green color in eastern tropical Pacific seafloor surface sediments is caused by the Fe (III) being reduced to Fe (II) in smectite clays. Löwemark et al. (2008) believed that the cyclical color variation in the central Arctic Ocean sediments was controlled by the Mn content in sediments. Cai et al. (2009) and Hu et al. (2012a) considered that hematite, goethite and Mn^{2+}-bearing calcite are the minerals imparting the red color based on the mineralogical studies on Cretaceous marine red shale and limestone, and hematite is one of the major coloring minerals.

The content of Fe- and Mn-bearing minerals in marine sediments are affected by many factors, including the biological effect (iron-bacterial mediation), sediment provenance, erosion pattern, geothermal condition and redox environment (Mamet & Préat, 2006; Ziegler & McKerrow, 1975; Schwertmann, 1971; Wang et al., 2009; Hu et al., 2012a; Jiang et al., 2019). Mamet & Préat (2006) considered that the red pigmentation of a number of Phanerozoic limestones is due to the dispersion of submicrometric (hydro) oxides (now hematite) formed by bacterial mediation during early diagenesis. Ziegler & McKerrow (1975) suggested that the main origin for the red color of Silurian marine sediment in the Western Europe and in the Appalachian Basin is caused by plentiful supply of oxidized Fe transported from land to sea. Schwertmann (1971; 1988) proposed that the hematite is preferentially formed in dry and warm conditions, because such a climate provides a favorable weak chemical weathering condition for the formation of hematite. Chen & Grapes (2007b) and Jiang et al. (2015; 2019) believed that the coloring of brown claystone in South China continent and SCS is related to elevated diagenetic temperatures. Wang et al. (2009) and Hu et al. (2012a) presented that the origin of Cretaceous marine red claystone is due to the iron oxidation in oligotrophic, highly oxic environment.

International Ocean Discovery Program (IODP) Expeditions 349, 367, 368 and 368X recovered pelagic brown claystone both in the northern continental margin and the oceanic basin in South China Sea (SCS), at Sites U1431, U1433, U1434, U1499, U1500, U1502 and U1503A (Li et al., 2014; Sun et al., 2018; Childress et al., 2020). Biostratigraphic studies show that the depositional age of these brown claystone is mostly in the Miocene, starting from about 23 Ma and ending at about 12 Ma (Li et al., 2014; Sun et al., 2018; Larsen et al., 2018; Childress et al., 2020), which provide an unprecedented opportunity to study the origin of pelagic brown claystone. Among these sites, U1503A was drilled at the oldest oceanic crust, and it contains a complete sequence of post-rifting marine sediment since early Oligocene. The color of the sediment changes from dark gray to brown and to gray again, which can constrain the complete duration of brown claystone in the SCS very well. Furthermore, there are several gray green interbeds in the brown claystone sequences, which make a perfect contrast with the brown claystone. In addition, the brown and green gray claystone from Site U1503A are weakly affected by diagenesis and turbidity currents. Therefore, U1503A is an ideal site to study the origin of the SCS pelagic brown claystone.

Considering the complexity of the genesis of marine red and brown claystone and its indications of the paleoclimate and paleo-ocean environment, we conducted grain size, clay minerals, major and trace elements, and Sr-Nd isotopic analyses on the brown and green claystone from Site U1503A to answer the following questions: (1) what may cause the U1503A sediments brown color during the early-mid Miocene, (2) what is the origin of the sediment color change from red to green, (3) does the brown claystone have any indications to the regional or global paleoclimate and paleo-ocean environment?

2. Geological background

SCS is the largest marginal sea in the western Pacific (Fig. 1). SE to nearly NS Cenozoic rifting resulted in the opening of the SCS. Seafloor spreading started at Oligocene (about 32 Ma) and ceased at Middle Miocene (about 15 Ma) (Li et al., 2014). Thereafter, the eastern part of the SCS began to subduct beneath the Philippine Sea Plate along the Manila Trench and caused the gradual uplift of Luzon arc(Liu et al., 2020; Huang et al., 2000). Meanwhile, northwestward movement of the Philippine Sea Plate towards the Asian continental marginal caused the formation of the Taiwan orogen (Huang et al., 2000; 2006).

With the development of Luzon arc and Taiwan orogen, a topographic barrier for deep water exchange between the SCS and the western Pacific was formed. The SCS deep basin became a semi-enclosed environment since late Miocene because of either closure of the connection with or temporary reduction of the western Pacific deep water flowing into the deep SCS (Chen et al., 2015). While, the benthic foraminiferal $\delta^{13}C$ results suggest that the SCS deep water and the western Pacific Deep Water (PDW) can be exchanged freely in the early-mid Miocene (Li et al., 2007; Chen et al., 2015). Furthermore, according to the benthic $\delta^{13}C$ and Nd isotope data from Pacific Ocean, it has been suggested that the deep water of Pacific was dominantly from Antarctic Bottom Water (AABW) during the early-mid Miocene (Wright et al., 1991; Ma et al., 2018).

The sediment inputs of SCS are controlled by surrounding continents and islands (Fig.1a). In the northern SCS, South China, Taiwan and Luzon islands are the proved to be major sediment sources; in the east, sediment input is mainly from Luzon islands; in the west, Red River and Indochina Peninsula control the sediment supply; in the south, sediment is mainly provided by Mekong River, Sumatra and Borneo (Liu et al., 2016). Considered that IODP Site U1503A is located in the northern SCS, the terrigenous detrital of U1503A may come from the South China,

Taiwan, and Luzon islands. However, the Taiwan would not be a significant provenance until its rapid uplift and exhumation after about 4 - 5 Ma (Hu et al., 2012; Clift et al., 2014). Hence, during the early-middle Miocene, the brown and green claystone from U1503A would be mainly provided by South China through Pearl River and Luzon islands.

3. Materials and methods

3.1. Materials

IODP Site U1503A is located in the northern SCS near the top of the structural high named Ridge C at 3867.7 m water depth (Fig.1a, c). Basalt was recovered in the basement and Ridge C was believed to be the oldest steady-state oceanic crust (Larsen et al., 2018; Sun et al., 2019). Lithostratigraphic Unit II (1484.74-1542.77 meters below seafloor) recovered about 18.53 meter due to the low recovery rate. This unit consists of 13.04 meter thick in total lithified dark brown massive claystone with a total of 5.49 m thick green gray intervals containing heavier bioturbation (Fig.1b). There are more than 10 green gray intervals, each with a thickness ranging from 2-89 cm. The green gray intervals are rich in foraminifer and other fossil fragments. A total of 46 samples were collected continuously at 40 cm intervals and at where the sediments color changes. The age framework of U1503A was established by the calcareous nannofossils and plankton-foraminifera in sediments (Childress et al., 2020). The sedimentary age of this unit is 22.14 - 14.24 Ma, and the sedimentary rate is 0.7 cm/kyr (Childress et al., 2020).

3.2. Methods

The redness and greenness degree of sediments are indicated by the reflectance a* of the Lab

color model. The value of reflectance a* below 5 means a green color, while above 5 means a red color. The reflectance a* of sediment was collected from IODP Expedition 368X Report (Childress et al., 2020).

After treated by excess 10% H_2O_2 and 0.5 mol/L HCl to remove organic materials and carbonates, terrigenous materials can be extracted. The grain size distribution of terrigenous fraction was measured with a Malvern Mastersizer 2000 at Key Laboratory of Ocean and Marginal Sea Geology, South China Sea Institute of Oceanology, Chinese Academy of Sciences. This instrument can measure grains in the 0.02-2000 μm range. The measurement repeatability is 0.5% for a single sample, and the reproducibility is better than 2% for duplicate samples. In this study, the end member (EM) algorithms improved by Paterson & Heslop (2015) was used to sort the grain size distributions into geologically meaningful end members.

The clay-sized fraction (< 2μm) was separating from the rest of the samples by application of Stokes' Law through settling. After 24 hours of saturated ethylene glycol vapor at 60 °C, the oriented slide with clay minerals was identified by X-Ray Diffraction (XRD) using a D8 ADVANCE diffractometer (made in Germany by Bruker AXS GmbH) at the Key Laboratory of Ocean and Marginal Sea Geology, South China Sea Institute of Oceanology, Chinese Academy of Sciences. Semi-quantitative estimates of peak areas of the basal reflection for the main clay mineral groups of smectite, illite, kaolinite and chlorite were carried out on glycolated samples using Jade software with the empirical factor of Biscaye (1965). The illite chemical index was estimated using the ratio of the 5 A˚ and 10 A˚ illite peak areas of ethylene-glycolated samples (Esquevin, 1969), while the illite crystallinity was estimated with the full width at half maximum of the illite 10 A˚ peak (Ehrmann, 1998).

The major and trace elements concentration were measured at the State Key Lab of Ore Deposit Geochemistry, Institute of Geochemistry, Chinese Academy of Sciences, Guiyang, using a Varian Vista Pro ICP-AES and a PerkinElmer Sciex ELAN 6000 ICP-MS respectively. Organic matter, carbonate and Fe-Mn oxides were removed using 10% H_2O_2 and 0.5 mol/L HCl respectively. The pretreated sample powder was dissolved by a mixture of 1 ml HF and 1 ml HNO3 in Teflon beakers. Details are given in Qi et al. (2000). Fe (II) content was calculated by the titration of potassium dichromate. Certified reference materials (GSR-3, GSR-5, GSR-6, OU-6, AGV-2, GBPG-1) were used for quality control. The analytical precision is better than 5% for major elements and 10% for trace elements. Enrichment factors (EF) were calculated to identify the enrichment or depletion of major and trace elements compared to the Average Shale (Wedepohl, 1971): $EF_{element}=(element/Al)_{sample}/(element/Al)_{Average\ Shale}$. The rare earth elements (REE) were normalized to chondrite composition (Sun & McDonough, 1989).

Twenty samples (ten brown and ten green samples) were measured for Sr-Nd isotopes compositions on a Neptune Plus MC-ICP-MS (Thermo Fisher Scientific, Dreieich, Germany) at the Wuhan Sample Solution Analytical Technology Co., Ltd., Hubei, China. After removing carbonate, Fe-Mn oxyhydroxide and organic fractions, all samples were digested in HNO_3-HF-$HClO_4$ mixtures. Sr and Nd were extracted by standard column procedures. Sr standard NBS 987 (Thirlwall, 1991) and Nd standard GSB04-3258-2015 (Li et al., 2017) were measured periodically to check the reproducibility and accuracy. The experimental error of the analyzed $^{87}Sr/^{86}Sr$ and $^{143}Nd/^{144}Nd$ is within ± 0.00001 and ± 0.000006, respectively. Nd results are expressed as $\varepsilon Nd = [(^{143}Nd/^{144}Nd_{sample})/(^{143}Nd/^{144}Nd_{CHUR})-1]*10000$, where the CHUR (Chondritic Uniform Reservoir) value is 0.512638 (Jacobsen & Wasserburg, 1980).

4. Results

The main grain size, clay minerals and geochemical results are presented in Figs. 2 to 5 and the data are given in Supplementary Table.

4.1. Terrigenous grain size

The grain size of terrigenous fraction is very fine, which is mainly composed of silt (40-65%, average 51%) and clay (35-60%, average 49%) (Fig.2). Green claystone is coarser than brown claystone. The end-member (EM) analysis shows that three EM models are the best optimization because of the high linear correlation index R^2 (above 0.9) and the low angular deviation (below 5). All EM have a clearly defined dominant mode. EM1, EM2 and EM3 have a modal grain size of 3μm, 4μm and 6μm respectively. The relative contributions of the EM1 varies between 15% and 73%, with an average of 41%, EM2 between 0 and 50%, with an average of 29%, and EM3 between 2% and 72%, with an average of 30%. The variation of EM2 shows a similar trend compared to the reflectance a*. After about 17 Ma, the percentages of EM3 increased and maintained at a high level.

4.2. Clay minerals

The clay mineral assemblages from measured section mainly consist of smectite (19-69%) with an average content of 41% and illite (21-58%) with an average content of 42%. Kaolinite (2-17%) and chlorite (2-19%) are present in lesser amount with average contents of 10% and 7%, respectively (Fig.3). From bottom to top, the content of smectite increases gradually, while the content of illite and kaolinite decreases. Although the clay mineral assemblages show a certain range of fluctuations, these fluctuations have no corresponding relationship with the change of

sediment color.

4.3. Geochemistry

The major element of samples consists mainly of SiO_2 (not measured) and Al_2O_3, with lower concentration of K_2O, Fe_2O_3, FeO, MgO, Na_2O, CaO, TiO_2, P_2O_5 and MnO (Fig.4). The content of total Fe ranges from 5.33-12.10% and it does not show much differences between brown and green claystone (Supplementary Table). While content of FeO (0.85-2.09%) and Fe_2O_3 (3.83-10.87%) shows high correlation with the sediment color change. The MnO (0.02-8.87%) and other major elements do not show corresponding relationship with sediment color change.

In terms of rare earth elements, as shown in Fig.5, the chondrite-normalized distribution patterns of REE are similar to those of Post Archean Australian Shales (PAAS). Samples and PAAS have similar LREE enrichment and Eu negative anomaly. There is no difference in chondrite-normalized distribution patterns of REE between brown and green claystone samples.

Sr-Nd concentrations and isotopic ratios are shown in Fig.7, Fig.8 and Supplementary Table. The Sr and Nd concentrations vary in 60.8-132 ppm and 24.1-38.8 ppm, respectively. The $^{87}Sr/^{86}Sr$ and ƐNd show a narrow range between 0.717628-0.730810 and -9.07--10.75, respectively. The Sr-Nd isotopic values show weak variations when the sediment color changes.

5. Discussion

5.1. The origin of brown color of the U1503A sediment

Previous studies on pelagic brown claystone in many regions show that the brown color of sediments is mainly controlled by Fe- or Mn- bearing minerals (Lyes, 1983; Löwemark et al., 2008; Cai et al., 2009; Hu et al., 2012a). Our results show that the sediment color in U1503

(reflectance a*) also show close relationship with the content of Fe_2O_3 and FeO (Fig.4). Compared with the green claystone, the brown claystone has higher content of Fe_2O_3 and lower content of FeO. The MnO concentration does not show clear correlation with the sediment color (Fig.4). Therefore, we suggest that the brown color of U1503A sediment is mainly caused by the higher content of Fe (III)- bearing minerals.

Among many Fe- bearing minerals, there are two main types that can make sediments red or brown, which are iron-rich smectite and Fe oxides (hematite or goethite) (Lyle, 1983; Hu et al., 2012a). For the iron-rich smectite, Fe is immobile and can be reduced or reoxidation easily (Lyle, 1983). The green pelagic sediments can turn into brown in a few minutes in peroxide condition (Lyle, 1983). However, in this study, the variations of Fe and smectite content in U1503A sediments are totally different (Fig.3, Fig.4), and the green claystone did not turn into brown after treated by 10% H_2O_2. This indicates that the iron-rich smectites are not the coloring media of the brown claystone in U1503A. Therefore, we suggest that the brown color of U1503A sediment in the early-mid Miocene should be attributed to the Fe oxides (hematite or goethite). More Fe (III) oxides result in brown coloring of sediments, while less Fe (III) oxides will cause sediment green or gray. This characteristic of Fe (III)-rich and Fe (II)-poor is also widely observed in marine red sediment from other regions, such as Cretaceous red shales in Tibet and Cretaceous red mudstone at ODP Site 641A (Hu et al., 2006; Wang, 2011). According to the measurement (Table 1), Fe_2O_3 in red/brown clayey sediment or claystone is usually higher than 7.5 %, and lower than 4.5 % in other color clayey sediments. While in limestone, much less content of Fe_2O_3 will generate reddish color.

5.2. The mechanism controlling the valence state of Fe in U1503A sediments

Since the content of total Fe does not show much differences between brown and green claystone, the valence state of Fe in U1503A sediments might be a key factor leading to the brown color. There are several factors that could affect the content or valence state of Fe in sediment, such as biological effect (iron-bacterial mediation) (Mamet & Préat, 2006), sediment provenance (Ziegler & McKerrow, 1975), erosion intensity (Schwertmann, 1971; 1988) and redox condition (Wang et al., 2009; Hu et al., 2012a). The biological effect can be excluded first in this study, because iron in sediments affected by the iron-bacterial mediation is not dispersed at random but is concentrated in a number of specific sedimentary features, like stromatolites and oncolites (Mamet & Préat, 2006). While brown claystone of U1503A is uniformly brown and there is no such sedimentary feature in U1503A (Childress et al., 2020). Therefore, we suggest that iron-bacterial has little effect on the variation of the valence state of Fe in U1503A. Other factors as sediment provenance, erosion intensity and redox condition are discussed in detail below.

5.2.1. Sediment provenance effect

The Pearl River and rivers from Taiwan and Luzon islands are the main sources of detrital sediments in the northern SCS (Hu et al., 2013; Liu et al., 2016). The sediments from other sources like the Mekong River and Red river are negligible because of the long transport distance and the topographic barriers during transportation (Liu et al., 2010; Liu et al., 2016). However, Taiwan may not be a sediment source until the rapid uplift of Taiwan at Late Miocene (Huang et al., 2006; Chen et al., 2015). Therefore, the main premise of provenance analysis is that the main sediment sources around the northern SCS during the early-mid Miocene can be limited between the South China and Luzon islands.

Three provenance analysis indexes were used to discriminate the provenance effect. First, the clay mineral assemblages were used, because the distribution of clay mineral assemblages in the SCS is primarily controlled by the clay mineral compositions of surrounding rivers (Liu et al., 2016; Wan et al., 2017). Sediment from Luzon rivers has a dominance of smectite, reflecting the eroding of the mafic volcanic bedrock (Liu et al., 2016). The modern Pearl River and the Holocene Pearl River from South China have totally different clay mineral assemblages. The modern Pearl River is more kaolinite-rich and smectite-poor compared with the Holocene Pearl River, suggesting an increased weathering and eroding caused by human activities (Hu et al., 2013; Clift et al., 2014). Clay mineral assemblages at U1503A samples are dominated by illite (42%) and smectite (41%) (Fig.3). Kaolinite (10%) and chlorite (7%) only account for a small percentage (Fig.3). As shown in the Fig.6, the clay mineral assemblages of U1503A samples are subparallel to the illite+chlorite-smectite line, suggesting a mixture of multiple sediment provenances from paleo-Pearl River and Luzon. Interestingly, samples are closer to the Luzon end member at 17-15 Ma. This can be explained with two different mechanisms, either due to provenance migration or due to different chemical weathering conditions (Chamley, 1989). More evidences are needed to judge which explanation is more appropriate. In general, what we can know from the clay mineral is that the South China and Luzon are the main sources of the early-mid Miocene sediments from U1503A, of which illite are mainly supplied by Pearl River and smectite are mainly provided by Pearl River and Luzon rivers..

Then, the REE results were analyzed, and which show that brown and green claystone samples at U1503A have highly similar Chondrite normalized REE distributions with PAAS (Fig.5), such as the common Eu depletion, LREE enrichment and relatively flat curves of HREE. The PAAS is

generally considered as the representative of the upper crust composition. The negative Eu anomaly means that volcanic or hydrothermal origin have little contribution to U1503A sediments. Therefore, we conclude that the highly coherency of REE variations indicate the similar sources of the brown and green claystone, and the chemical weathering condition may lead to the variation of clay mineral assemblages.

Finally, Sr-Nd isotope was utilized, and which is a more robust indicator of sediment provenance in marine sediments than clay minerals and REE.(Clift et al., 2014; Wan et al., 2017). The Nd isotope composition is not affected by the chemical weathering and transport process, but only controlled by the lithology and geologic age of source rocks (Goldstein et al., 1984; Wan et al., 2017). Although the previous studies show that the chemical weathering and grain size have influence on the silicate $^{87}Sr/^{86}Sr$ value (Chen et al., 2007a; Hu et al., 2013), we suggest that these effects can be negligible here. The main reason is that the sediment at U1503A has very fine grain size (mainly composed of silty clay) and the grain size shows low correlation with $^{87}Sr/^{86}Sr$ values (Fig.7a), suggesting the insignificant influence of grain size on Sr isotope compositions. The $^{87}Sr/^{86}Sr$ values of U1503A samples vary in a narrow range (Fig.8) and do not show the same trend as the typical chemical weathering proxies (e.g., CIA, Al/K). Therefore, $^{87}Sr/^{86}Sr$ and ƐNd can be used to further constrain the provenance of U1503A sediments. Fig.7b shows the field into which all U1503A samples fall compared with data from the modern Pearl River (Liu et al., 2007), Holocene Pearl River (Hu et al., 2013) Luzon rivers (Goldstein & Jacobsen, 1988), and modern SCS seafloor surface (Liu et al., 2016). The $^{87}Sr/^{86}Sr$ and ƐNd of U1503A samples distribute in a relatively concentrated area and lie close to the mixing line of Luzon and modern Pearl River (Fig.7b), suggesting that sediment provenance is stable. Therefore, the 17-15 Ma samples closer to

the Luzon in clay mineral source discrimination diagram (Fig.6) is not due to the provenance change, but may be due to different chemical weathering conditions.

Based on the above discussion on clay mineral, REE and Sr-Nd isotope, we can conclude that the early-mid Miocene U1503A sediments have stable provenances, and the detrital sediments mainly come from South China (Pearl River) and Luzon. The relatively stable provenance means that sediment provenance has little influence on the variation of Fe (II) and Fe (III) concentration. Hence, the valence state of Fe from U1503A sediments may be controlled by other factors.

5.2.2. Erosion intensity effect

Geochemistry, grain size and clay minerals have been widely used for measuring the strength of erosion in marine sediments (Clift et al., 2014; Wan et al., 2009; 2017). In this paper, the chemical index of alteration (CIA), EM3, Ti/Na, Al/K, smectite/(illite+chlorite) and $^{87}Sr/^{86}Sr$ are used to reconstruct the intensity of weathering. CIA is based on the hypothesis that relative mobile elements (Ca, K, Na) will be leached during alteration, whereas the immobile element Al remains concentrated in residues of weathered rocks (Nesbitt & Young, 1982). CIA is defined as $100*Al_2O_3/(Al_2O_3+CaO^*+Na_2O+K_2O)$, which is calculated with molecular weights of oxides (Nesbitt & Young, 1982). CaO* means the CaO content in the silicate fraction of the sample. Ti/Na and Al/K are also the sensitive chemical weathering indictors, because alkali elements, like Na and K, are relatively mobile in water, while the Ti and Al are less mobile during the breakdown of the minerals (Nesbitt et al.,1997; Clift et al., 2014). Smectite and kaolinite are formed by chemical alteration, while illite and chlorite are formed by physical erosion or weathering under moderate hydrolysis conditions (Chamley, 1989). Stronger weathering is indicated by higher ratios of smectite and kaolinite over illite and chlorite (Chamley, 1989; Hu et al., 2013). When the

source is stable, $^{87}Sr/^{86}Sr$ is used to reconstruct the chemical weathering, with higher $^{87}Sr/^{86}Sr$ meaning stronger alteration (Hu et al., 2013; Clift et al., 2014). Although previous studies show that hydraulic sorting may also influence the sedimentary elemental ratios, Wan et al. (2007, 2009) indicated that there is no significant influence of sea level change on the sedimentation at ODP Site 1146 based on the lack of correlation between terrigenous MAR, grain-size, and global sea-level since 20 Ma. Compared with ODP Site 1146, IODP Site U1503A is deeper and located further oceanward, which means that the hydraulic sorting effect on sedimentary elemental ratios can also be negligible at Site U1503A samples.

In terms of grain size, the end member analysis can be used to sort the grain size distributions into geologically meaningful end members (Paterson & Heslop, 2015). Sediment grain size end members are also good proxy of erosion intensity (Wan et al., 2007; He et al., 2020). At Site U1503A, EM3 (average: 30%) and EM1 (average: 41%) are the coarsest and finest sediments, respectively. In previous studies, such as offshore Nambia (Stuut et al., 2002), continental slope of the northern SCS (Wan et al., 2007), and northern Arabian Sea (He et al., 2019), the coarsest (except the turbidity sediment) and the finest end member of bathyal-abysmal sediments was usually interpreted as eolian dust and fluvial mud. Wan et al. (2007) suggest that the coarsest end member of ODP Site 1146 in the northern SCS have the similar grain-size distributions compared with typical loess samples. And the Pearl River supplies about 84.3 Mt/year sediment to the SCS (Zhang et al., 2012), meaning that the major terrigenous sediment input of northern SCS should be of fluvial origin (Li et al., 2003; Wan et al., 2007). Hence, in this paper, the coarsest EM3 and the finest EM1 were also interpreted as eolian dust and fluvial origin, respectively. EM2 (average: 29%) is the intermediate end-member. Shao et al. (2007) suggested that there is a strong bottom

current along the northern SCS margin according to the seismic profile analyses (drift sediment accretion). The existence of bottom current is also supported by the temporal and spatial variability of clay mineral assemblages in sediments from northern SCS (Liu et al., 2010). Similarly, sedimentary magnetic properties suggest a strong deep water current at Last Glacial Maximum in the northern SCS (Zheng et al., 2016). Furthermore, the bottom current in the northern SCS, a branch of West Pacific Ocean Current, would be more controlled by the West Pacific deep water during the early-mid Miocene because the subduction-collision event in Taiwan region and uplift of Luzon Strait did not occur and the SCS basin was open to the Pacific (Li et al., 2007; Chen et al., 2015). Hence, the sediment transport process by bottom current in the northern SCS should also be considered. The intermediate EM2 can be reasonably considered as deep water current origin.

According to above discussion, the weathering proxies (CIA, EM3 (eolian dust), Ti/Na, Al/K, smectite/(illite+chlorite) and $^{87}Sr/^{86}Sr$) can be used to indicate the variation of erosion intensity. As shown in the Fig.8, the very similar trends of CIA, Ti/Na, Al/K, smectite/(illite+chlorite) at Site U1503A indicate an overall rising trend in chemical weathering intensity in South China during the early-mid Miocene. Most samples have a high value of CIA (>80), which suggest an extremely strong weathering condition on the whole (Fedo et al., 1995). Since about 17 Ma, all values of these chemical weathering proxies (CIA, Ti/Na, Al/K, smectite/(illite+chlorite)) increase abruptly and maintain at a higher level, which can be interpreted as a stronger chemical weathering environment, such as stronger summer monsoon with warmer temperature and higher precipitation. Furthermore, EM3 (eolian dust), which usually can be associated with physical erosion (Wan et al., 2007), also show the similar variations with above chemical weathering

proxies. The high values of EM3 (eolian dust) since 17 Ma indicate that physical erosion was also enhanced. However, the $^{87}Sr/^{86}Sr$ values are relatively stable and do not increase like other proxies, possibly suggesting the non-uniqueness about the interpretation of seawater strontium isotope ratio (Wan et al., 2009).

Because the sediment source did not change at the early-mid Miocene, we can conclude that the source had gone through stronger chemical weathering and physical erosion since 17 Ma based on the multiple erosion indicators. This conclusion has also been supported by analyses of clay mineral and geochemistry of sediments at ODP Site 1146 and 1148 (Wan et al., 2009; Clift et al., 2014), and regional seismic reflection profile analysis through the Asian marginal seas (Clift, 2006). According to the $\delta^{18}O$ record of Miller et al. (2020), 17-13.8 Ma was the Miocene Climatic Optimum (MCO) with the warmest climate since the early Oligocene. As shown in the Fig.8, the enhanced erosion and the MCO occurred at the same time. Considering that there is no strong tectonic movement in the SCS region during the early-mid Miocene (Sun et al., 2009; 2014), the global MCO (high temperature and strong precipitation) maybe the major mechanism to cause increased erosion.

Schwertmann (1971; 1988) suggested that dry and warm climate is conducive to the formation of hematite. Hu et al. (2012b) and Clift et al. (2014) use hematite/goethite as an indicator of dry winter monsoon. Hematite is normally considered as the key determinant for the red and brown colors in many marine brown claystone (Cai et al., 2009; Hu et al., 2012a). It means that dry and warm climate will lead to more hematite formation, which in turn will cause red and brown coloring of sediments. However, compared with sediment color and multiple erosion intensity indicators in this study, we don't find such correlation (Fig.8). For example, since the 17 Ma, both

physical and chemical weathering were intensified. It indicates a seasonal climate with dry periods between summer rains which is in favour of hematite formation. However, the sediment does not show redder than they were before the 17 Ma (Fig.8). Hence, we suggest that the valence state of Fe from U1503A sediments are not controlled by the erosion intensity.

5.2.3. Redox condition effect

The above-mentioned discussions indicate that Fe oxides are unlikely affected by the factors as iron-bacterial mediation, sediment source and erosion intensity. However, we are still not sure whether the Fe oxides (hematite or goethite) are derived from continental weathering or formed during syn-sedimentary or early diagenetic processes. To address this question, a correlation of Fe_2O_3 and FeO with Al_2O_3 and TiO_2 (Fig.9) was analyzed. Al_2O_3 and TiO_2 are commonly used as a representative of terrestrial fraction because both elements are relative immobile and not so vulnerable to authigenesis or analytical errors (Clift et al., 2014). In the case that source and erosion don't have much influence on Fe oxides, Fe_2O_3 and FeO would show positive linear correlation with Al_2O_3 and TiO_2 if authigenesis and diagenetic processes are limited. However, as shown in Fig.9, cross-plot of Fe_2O_3 and FeO versus Al_2O_3 and TiO_2 reveal a low covariation trend. This indicates that authigenesis and diagenetic processes had affected the Fe (III) and Fe (II) content strongly. Furthermore, Fe_2O_3 and FeO display no obvious correlation with grain size, excluding the effect of grain size on the iron valence state. Hence, iron content from U1503A brown and green claystone are foremost controlled by authigenic phases, meaning that redox condition is the main cause of Fe changes in valence state. We suggest that iron imported from terrestrial sources underwent transformation during syn-sedimentation and diagenesis process under the influence of the redox environment.

In order to distinguish the redox environment difference between the brown and green claystone, some of the redox sensitive elements (Ni, Co, V, Cr, U) are used as indicators of redox condition because the solubility of these elements is strongly dependent on the redox gradients established within the water column and/or below the sediment-water interface (Jones & Manning, 1994; Ferreira et al., 2020). In this paper, Ni/Co, U/Th, V/Cr, and U_{au} (authigenic U= total U-Th/3) are used to estimate benthic redox condition. Ni/Co has been suggested as an index of oxygenation in several studies, because both Ni and Co are relatively enriched in reducing condition and they show a certain content correlation due to the differences of their geochemical behaviors (Jones & Manning, 1994; Tribovillard et al., 2006). Jones & Manning (1994) suggested high value of Ni/Co reflects reducing condition, while oxic sediment has Ni/Co < 5, dysoxic sediments between 5 and 7, and anoxic sediments > 7. V/Cr has also been used as a redox index. Although Cr could be exported to sediments under anoxic condition because it can readily complex with humic/ fulvic acids or adsorb Fe- and Mn-oxyhydroxides, Cr is usually incorporated within the detrital clastic fraction due to the large amount of Cr in the land source input (Jones & Manning, 1994; Tribovillard et al., 2006). Whereas, V is usually bound to organic matter and concentrated in reducing conditions (Jones & Manning, 1994; Tribovillard et al., 2006). V/Cr value above 4.25 represents anoxic environment, and the oxic to dysoxic transition occur at a V/Cr value of 2 (Jones & Manning, 1994). U/Th and U_{au} are also sensitive redox condition indicators, with high value of U/Th and U_{au} representing reducing condition. Th is independent of redox environments since Th is relatively immobile and usually found in detrital fraction, whereas reducing conditions could cause more authigenic U insolubile and fixed, leading to increasing overall U/Th and U_{au} (Jones & Manning, 1994, Tribovillard et al., 2006). According to Jones & Manning (1994), U/Th of 1.25

and U_{au} of 12 are used as the thresholds of dysoxic and anoxic conditions, and U/Th of 0.75 and U_{au} of 5 are the thresholds of oxic and dysoxic conditions.

However, before the above redox sensitive elements be used to identify the redox condition of sediments, terrestrial detrital effect and hydrothermal sources effect (non-authigenic element) must be excluded. As discussed above, U1503A has obvious negative Eu anomaly and show similar trends of chondrite normalized REE patterns with PAAS (McLennan, 1989) (Fig.5), suggesting that the sediments are mainly from the upper continental crust. Therefore, the contribution from hydrothermal sources can be neglected. The detrital sources effect can also be excluded in this study according to the correlation analysis of these redox sensitive elements with Al. As shown in Fig.10, there is no significant correlation between trace elements (Ni, Co, V, Cr, U) and Al, suggesting that these trace elements are strongly affected by authigenic diagenesis process rather than by the detrital flux. Hence, elements Ni, Co, V, Cr, U can be used for redox condition analysis.

As shown in the Fig.10, the results of redox environment discrimination demonstrate that although there are few samples fall into the field of dysoxic condition, most samples plot within the field of oxic condition. This means that both brown and green claystone from U1503A were deposited under overall oxic environment. Furthermore, the above redox sensitive elements (except Cr) are more depleted in brown than green claystone from U1503A above the background established by the Average Shale (Fig.11), indicating the more oxygen-rich condition of brown claystone than that of green claystone. The EF_{Cr} shows different characteristics from other redox elements, which probably because Cr could be strongly influenced by detrital sources (Jones & Manning, 1994; Tribovillard et al., 2006). Hence, we suggest that although both brown and green

claystone are deposited under oxic environment at the sediment-water interface, the sedimentary condition of brown claystone are more oxygen-rich. This difference in redox conditions caused the variation of iron valence state, and finally leads to the variation of sediment color.

5.3. The reason of redox condition change in SCS during the early-mid Miocene

Based on the above discussion, we can conclude that the color of U1503A sediment is mainly controlled by the redox condition at the sediment-water interface. This raises a new question: what caused the redox condition change during the early-mid Miocene? Previous studies suggested that sedimentary rate or paleo-productivity, geo-temperature, and deep water current have significant effects on the redox condition of sediments (Lyes, 1983; Glasby, 1991; Li et al.,2007; Jiang et al., 2019; Hu et al., 2012a). Low sedimentary rate or low primary productivity can stimulate the oxidation of iron, and resulted in the deposition of brown clays in modern Pacific (Lyes, 1983; Glasby, 1991). However, in this study, sedimentary rate of U1503A during the early-mid Miocene is around 0.67cm/kyr (Childress et al., 2020), which is 10^2 times higher than that of the modern Pacific brown clays (around 0.01 cm/kyr). Meanwhile, the Ba/Al value, which is considered to be a paleoproductivity proxy due to the positive correlation with primary productivity (Dymond et al., 1992; Tribovillard et al., 2006), is similar in brown and green claystone of U1503A (Supplementary Table). Therefore, neither sedimentary rate nor primary productivity is responsible for the redox condition of the brown and green claystone at U1503A. In terms of geothermal effect, Jiang et al. (2019) suggested that the high oxygen fugacity environment in IODP Site U1434 brown beds originated from high geo-temperature during sedimentary-diagenesis process because of directly depositing on recently erupted basalts. However, we consider the oxic condition of U1503A sediment was not caused by the high geo-temperature according to the following three points of evidence: (1) the U1503A brown claystone

are not directly deposited on the basalt basement. There are about 55 meters of gray claystone and dark gray chalk between the basalt basement and the brown claystone, which is classified as Unit III (Childless et al, 2020). If the high geo-temperature caused the oxic condition for U1503A brown claystone, such brown claystone should also occur in Unit III because they are closer to the basement and have the similar mineral composition; however, this is not observed. (2) more than ten layers of green interbeds occur in the research period, and which do not support the one-dimensional geo-temperature scenario. (3) the high geo-temperature during diagenesis process would not only promote the formation of hematite (Gialanella et al., 2010; Jiang et al., 2019), but also cause conversion of smectite to illite due to dehydration (Hower et al., 1976; Mevinier et al., 2004). However, compared with the green claystone, the illite content of brown samples does not increase, suggesting that high geo-temperature might not work (Fig.3).

After excluding the influence of sedimentary rate, primary productivity and geo-temperature, the change of deep water current became a most plausible factor. As indicated by the results of grain size end-member analysis (Fig.2), the EM2, representing the bottom current transport origin, shows a highly consistent content variation with sediment color (reflectance a*). The brown claystone has higher percentage of EM2, meaning a stronger bottom current, while the green claystone has the lower percentage of EM2, meaning a weaker bottom current. The highly consistent variation between EM2 and sediment color suggest that the variation of oxygen-rich deep water current may control the redox conditions of U1503A sediments during the early-mid Miocene.

Similar results are supported by studies on the data of physical property, benthic foraminifera, and stable isotopes from ODP Sites 1148, 1146, and 1143 in SCS (Li et al., 2007). The red brown

sediments in the SCS since the early Miocene have positive red parameter (a*), low content of $CaCO_3$, more benthic species which prefer oxygen-rich bottom conditions, representing well ventilation in deep water (Li et al., 2007). Jin et al. (2020) came to the analogous conclusions according to analysis on IODP Site U1502 sediments in the SCS since the Late Miocene. The sediment color reflectance, nannofossil, key element content, and clay minerals suggested that the occurrence of the cyclicity-like brown to green transition in U1502 could result from the extent of deep water ventilation, which is possibly related with deep oceanic circulation (Jin et al., 2020). Hence, we conclude that the redox condition change in U1503A sediments during the early-mid Miocene was controlled by the strength of oxygen-rich bottom current in the SCS basin. Strong bottom current could bring high concentration of oxygen, which cause oxic condition in the deep water and is favorable for the deposition of brown claystone. While weak bottom current cause poor ventilation in deep water, which form less Fe (III) oxides and cause the green claystone deposit (Fig. 13).

5.4. Implication to deep water circulation

Based on the above discussions and previous studies (Li et al., 2007; Hu et al., 2012a; Jin et al., 2020), we suggest that the brown and green claystone of U1503A could reflect the variations of circulation and deep water ventilation in the northern SCS. Furthermore, considering that the deep water current of SCS has strong connection with the West Pacific deep water circulation, we speculate that the transition of U1503A sediment color may have wide implication to large-scale ocean current changes.

During the early-mid Miocene, the SCS was open to the western Pacific because the northwest migration of Luzon arc and collision between the Eurasian Plate and the Philippine Plate had not

occurred yet (Huang et al., 2000; Chen et al., 2015). The well fit between SCS and Pacific benthic $\delta^{13}C$ curve during the Miocene indicates that the deep water of the SCS and the western Pacific could be exchanged freely during this period (Li et al., 2006; Chen et al., 2015). The Miocene circulation patterns were greatly different from the modern ones (Holbourn et al., 2013). The benthic $\delta^{13}C$ and Nd isotope data suggest that the deep water of Pacific was dominantly supplied by the Southern Ocean during the early-mid Miocene (Wright et al., 1991; Ma et al., 2018), which differed greatly from the modern Pacific deep water because the northern hemisphere was relatively warm and the North Atlantic Deep Water formation remained weak until the late Miocene (Butzin et al., 2011; Holbourn et al., 2013). Hence, during early-mid Miocene, the ventilation of the western Pacific would be strongly affected by the strength of AABW. And cold climate would be in favour of the AABW formation (Talley et al., 2013; Holbourn et al., 2013; Ferrari et al., 2014). Holbourn et al. (2013) suggest that the increased benthic foraminifers and Log(Mn/Ca) during the middle Miocene colder episodes in the Pacific Ocean indicate improvement of deep water ventilation and intensification of AABW. Similar results were also presented by Ferrari et al. (2014) according to the expansion of Antarctic origin water volume at the Last Glacial Maximum, and by Butzin et al. (2011) according to the modeling outcomes of increased Pacific deep water production linked to the cooling of Antarctica at the middle Miocene. Therefore, it is reasonable to infer that the cold episodes in early-mid Miocene would lead to Antarctic ice sheet expansion and stronger north-ward AABW than other stages, which may in turn cause better ventilation in SCS and western Pacific deep water.

Because of the low recovery rate and poor $CaCO_3$ reservation at U1503A brown claystone, the benthic $\delta^{18}O$ records of adjacent ODP Site 1148 (Cheng et al., 2004) is utilized as a reference to

that of U1503A. As shown in the Fig.12, the ventilation proxies (reflectance a*, EM2 and Fe^{3+}/TFe) of SCS and $\delta^{18}O$ of Site 1148 and Pacific varied in the same pace. The green intervals were mainly deposited during the warmer periods ($\delta^{18}O$ decreases), while the brown claystone were mainly developed during the colder periods ($\delta^{18}O$ increases). This indicates that ventilation of the SCS deep water would be strongly affected by the strength of the AABW. Therefore, the sediment color of brown or green at U1503A was conjectured to be related with the expansion or reduction of AABW volume due to the glacial-deglacial cycles in early-mid Miocene. During the glacial stages (Fig.13a), more oxygen-rich south-sourced deep water flow into the SCS. Consequently, the deep water in the SCS could be well-ventilated, causing the brown coloring of sediments. While during the deglacial stages (Fig.13b), the southern-sourced deep water volume decreased, resulting in lower content of dissolved oxygen in the SCS deep water which in favour of deposition of green claystone. We suggest that the brown to green variations in U1503A sediment have significant implications to the ventilation in SCS deep water and to the Pacific Ocean circulation changes. It is an important evidence for the changes in AABW circulation caused by the glacial-deglacial cycle during the early- mid Miocene.

The deposition of brown sediment in the SCS started at about 23 Ma, which corresponds with the southwestward shift of SCS spreading ridge. The tectonic movement caused the acceleration of seafloor spreading. The depth of central sea basin exceeded 3000 m (Li et al., 2007; Jian et al., 2019). Since then, the oxygen-rich deep water of the western Pacific could enter the SCS deep-sea basin, resulting in the oxic sedimentary environment in deep-sea basin and the deposition of brown sediment. After middle Miocene, with the growth of Luzon arc and Taiwan, the poor connection of deep water between the SCS and western Pacific caused the isolation and which in

turn the poor ventilation of the SCS deep basin (Chen et al., 2015). The low concentration of oxygen in deep SCS may lead to the gradually reduction and finally extinct of brown claystone thereafter.

6. Conclusion

Based on the analyses of reflectance a*, grain size, clay minerals, major and trace elements, and Sr-Nd isotope properties of brown and green claystone during the early-mid Miocene from IODP Site U1503A in the northern SCS, we discussed the origin of the sediment color transition and their implications to the deep water circulation. The main conclusions include:

(1) The early-mid Miocene (22.14-14.24 Ma) sediment from IODP Site U1503A is composed of 13.04 m thick dark brown claystone and 5.49 m thick green gray claystone interbeds. The brown and green claystone have similar contents of total iron, while the Fe (III) content in brown claystone is significantly higher than that of adjacent green claystone. We suggest that the relatively high content of Fe (III) oxides caused the brown color of sediment.

(2) The U1503A sediment had relatively stable provenances during the early-mid Miocene, which are mainly supplied by South China (Pearl River) and Luzon islands. The provenance had undergone strong chemical and physical erosion since 17Ma, which may be associated with climate changes during the Miocene Climatic Optimum. After excluding effects of iron-bacterial mediation, sediment source, and erosion intensity, we inferred that the brown claystone may reflect more oxic sedimentary conditions than interbeded green claystone.

(3) Considering the synchronous variation of ventilation proxies (reflectance a*, EM2 and Fe^{3+}/TFe) of SCS and $\delta^{18}O$ of Site 1148 and Pacific, we supposed that this kind of oxic

environment should be associated with the relative strong oxygen-rich deep water current. During the glacial period, the more oxygen-rich and stronger bottom current from Antarctic would bring high concentration of oxygen into the SCS through deep water current, which caused oxic sedimentary condition and brown coloring of U1503A sediments. While during the deglacial period, the Antarctic ice sheet reduced and the formation of AABW was decreased. The SCS deep water would contain relatively low concentration of oxygen, which in turn would favour the formation of green claystone.

Acknowledgement

Samples, age framework, reflectance a* data and core photos in this paper are provided by the International Ocean Discovery Program (IODP). We are grateful to the cruise members and scientists of JOIDES resolution during IODP Expeditions 367, 368 and 368X. We thank Jianguo Liu for providing us insightful suggestions on the figures and paper structures. This work was supported by K.C. Wong Education Foundation (GJTD-2018-13), Guangdong NSF research team project (2017A030312002) and Key Special Project for Introduced Talents Team of Southern Marine Science and Engineering Guangdong Laboratory (Guangzhou) (GML2019ZD0104; 2019BT02H594; GML2019ZD0205). The data used in this paper was uploaded to the system in the supporting information. They will be open for public along with the publication of this paper. The data in this paper are available at the Figshare website (https://figshare.com/s/d1fb4acd9105d908e347). We declare no competing interests.

References

Biscay, P. (1965). Mineralogy and sedimentation of recent deep−sea clay in the Atlantic Ocean and adjacent seas and oceans. *Geological Society of America Bulletin*, 76, 803-832.

Butzin, M., Lohmann, G., & Bickert, T. (2011). Miocene ocean circulation inferred from marine carbon cycle modeling combined with benthic isotope records. *Paleoceanography*, 26, PA1203. http://dx.doi.org/10.1029/2009PA001901

Cai, Y.F., Li, X., Hu, X.M., Chen, X.M., & Pan, Y.G. (2009). Paleoclimatic approach to the origin of the colouring of Turonian pelagic limestones from the Vispi Quarry section (Cretaceous, central Italy). *Cretaceous Research*, 30 (5), 1205-1216.

Chamley H. (1989). *Clay Sedimentology.* Berlin: Springer-Verlag.

Chen, J., Li, G.J., Yang, J.D., Rao, W.B., Lu, H.Y., Balsam, W., et al. (2007a). Nd and Sr isotopic characteristics of Chinese deserts Implications for the provenances of Asian dust. *Geochimica et Cosmochimica Acta*, 71, 3904-3914.

Chen, G.N., & Grapes, R.H. (2007b). *Granite Genesis: in-situ Melting and Crustal Evolution*, Berlin, Heidelberg, Dordrecht: Springer-Verlag.

Chen, W.H., Huang, C.Y., Lin, Y.J., Zhao, Q., Yan, Y., Chen, D., et al. (2015). Depleted deep South China Sea $\delta^{13}C$ paleoceanographic events in response to tectonic evolution in Taiwan–Luzon Strait since Middle Miocene. *Deep-Sea Research Part II-Topical Studies in Oceanography*, 122, 195-225.

Cheng, X., Zhao, Q., Wang, J., Jian, Z., Xia, P., Huang, B., et al. (2004). Data report: Stable isotopes from Sites 1147 and 1148. In Prell, W.L., Wang, P., Blum, P., Rea, D.K., and Clemens, S.C. (Eds.), Proceeding of the Ocean Drilling Program, Scientific Results, 184. http://www-odp.tamu.edu/publications/184_SR/223/223.htm

Childress, L.B., Alvarez Zarikian, C.A., Briais, A., Dadd, K.A., Deng, J.-M., Höfig, T.W., et al. (2020). Return to Site U1503. In Sun, Z., Jian, Z., Stock, J.M., Larsen, H.C., Klaus, A., Alvarez Zarikian, C.A., and the Expedition 367/368 Scientists, South China Sea Rifted Margin. Proceedings of the International Ocean Discovery Program, 367/368: College Station, TX (International Ocean Discovery Program). https://doi.org/10.14379/iodp.proc.368X.103.2020

Clift, P. D. (2006). Controls on the erosion of Cenozoic Asia and the flux of clastic sediment to the ocean, *Earth and Planetary Science Letters*, *241*, 571-580.

Clift, P. D., Wan, S. M., & Blusztajn, J. (2014). Reconstructing chemical weathering, physical erosion and monsoon intensity since 25 Ma in the northern South China Sea: a review of competing proxies. *Earth-Science Reviews*, *130*, 86-102.

Dymond, J., Suess, E., & Lyle, M. (1992). Barium in deep-sea sediment: a geochemical proxy for paleoproductivity. *Paleoceanography*, *7*(2), 163-181.

Ehrmann, W. (1998). Implications of late Eocene to early Miocene clay mineral assemblages in McMurdo Sound (Ross Sea, Antarctica) on paleoclimate and ice dynamics. *Palaeogeography Palaeoclimatology Palaeoecology*, *139*, 213-231.

Esquevin, J. (1969). Influence de la composition chimique des illites sur leur cristallinit?? *Bulletin des Centres de Recherches Pau−SNPA*, *3*, 147-153.

Fedo, C.M., Nesbitt, H.W., & Young, G.M. (1995). Unraveling the effects of potassium metasomatism in sedimentary rocks and paleosols, with implications for paleoweathering conditions and provenance. *Geology*, *23*, 921-924.

Ferreira, E., Mateus, A., Azerêdo, A.C., Duarte, L.V., Mendonça-Filho, J., & Tassinari, C.C.G. (2020). Tracing bottom-water redox conditions during deposition of Lower and Upper Jurassic organic-

rich sedimentary rocks in the Lusitanian Basin (Portugal): Insights from inorganic geochemistry. *Marine and Petroleum Geology*, *117*.

Gialanella, S., Girardi, F., Ischia, G., Lonardelli, I., Mattarelli, M., & Montagna, M. (2010). On the goethite to hematite phase transformation. *Journal of Thermal Analysis and Calorimetry*, *102*(3), 867-873.

Glasby, G.P. (1991). Mineralogy, geochemistry, and origin of Pacific red clays: a review. *New Zealand Journal of Geology and Geophysics*, *34*(2), 167-176.

Goldstein, S.L., O'Nions, R.K., & Hamilton, P. J. (1984). A Sm– Nd isotopic study of atmospheric dusts and particulates from major river systems. *Earth and Planetary Science Letters*, *70*, 221-236.

Goldstein, S.J., & Jacobsen, S.B. (1988). Nd and Sr isotopic systematics of riverwater suspended material -implications for crustal evolution. *Earth and Planetary Science Letters*, *87*, 249-265.

He, W., Liu, J., Huang, Y., & Cao, L. (2020). Sea level change controlled the sedimentary processes at the Makran continental margin over the past 13,000 yr. *Journal of Geophysical Research: Oceans*, *125*, e2019JC015703.

Holbourn, A., Kuhnt, W., Frank, M., & Haley, B.A. (2013). Changes in Pacific Ocean circulation following the Miocene onset of permanent Antarctic ice cover. *Earth and Planetary Science Letters*, *365*, 38-50.

Hu, D.K., Boning, P., Kohler, C.M., Hillier, S., Pressling, N., Wan, S.M., et al. (2012b). Deep sea records of the continental weathering and erosion response to East Asian monsoon intensification since 14 ka in the South China Sea. *Chemical Geology*, *326*, 1-18.

Hu, D.K., Clift, P.D., Boning, P., Hannigan, R., Hillier, S., Blusztajn, J., et al. (2013). Holocene evolution in weathering and erosion patterns in the Pearl River delta. *Geochemistry Geophysics Geosystems*, *14*, 2349-2368.

Hu, X.M., Wang, C.S., Li, X.H., & Luba, J. (2006). Upper Cretaceous oceanic red beds in southern Tibet: lithofacies, environments and colour origin. *Science in China Series D: Earth Sciences*, *49* (8), 785-795.

Hu, X., Scott, R.W., Cai, Y., Wang, C., & Melinte-Dobrinescu, M.C. (2012a). Cretaceous oceanic red beds (CORBs): different time scales and models of origin. *Earth-Science Reviews*, *115*(4), 217-248.

Huang, C.Y., Yuan, P.B., Lin, C.W., Wang, T.K., & Chang, C.P. (2000). Geodynamic processes of Taiwan arc–continent collision and comparison with analogs in Timor, Papua New Guinea, Urals and Corsica. *Tectonophysics*, *325*, 1-21.

Huang, C.Y., Yuan, P.B., & Tsao, S.J. (2006). Temporal and spatial records of active arc– continent in Taiwan: a synthesis. *Geological Society of America Bulletin*, *118*, 274-288.

Jacobsen, S.B., & Wasserburg, G.J. (1980). Sm–Nd isotopic evolution of chondrites. *Earth and Planetary Science Letters*, *50*, 139-155.

Jian, Z., Jin , H., Kaminski, M.A., Ferreira, F., Li, B., & Yu, P.-S. (2019). Discovery of the marine Eocene in the northern South China Sea. *National Science Review*, *6*, 881-886. https://doi: 10.1093/nsr/nwz084

Jiang, L.T., Chen, G. N., Grapes, R., & Peng, Z. L. (2015). Thermal origin of continental red beds in SE China: An experiment study. *Journal of Asian Earth Sciences*, *101*(2015), 14-19.

Jiang, L.T., Sun, J., Hu, L.T., Zhan, W.H., Tang, Q.Q., & Li, J. (2019). The genesis and geological implications for oceanic redbeds of the South China Sea in U1434 of IODP Expedition 349—the

constraint from diffuse reflectance and X-ray fluorescence spectroscopy. *Spectroscopy and Spectral Analysis*, *39*(4), 1294-1300.

Jin, X., Xu, J., Li, H., Li, Y., Qiao, P., Wu, L., et al. (2020). Origin of the rhythmic reddish-brown and greenish-gray sediments in the abyssal South China Sea: Implications for oceanic circulation in the late Miocene. *Marine Geology*, *430*.

Jones, B., & Manning, D. A. C. (1994). Comparison of geochemical indices used for the interpretation of palaeoredox conditions in ancient mudstones. *Chemical Geology*, *111*, 111-129.

Larsen, H.C., Sun, Z., Stock, J.M., Jian, Z., Alvarez Zarikian, C.A., Klaus, A., & the Expedition 367/368 Scientists (2018). Proceedings of the International Ocean Discovery Program, South China Sea Rifted Margin, (Vol. 367/368). College Station, TX: International Ocean Discovery Program. https://doi.org/10.14379/iodp.proc.367368.101.2018

Li, C.-F., Xu, X., Lin, J., Sun, Z., Zhu, J., Yao, Y., et al. (2014). Ages and magnetic structures of the South China Sea constrained by deep tow magnetic surveys and IODP Expedition 349. *Geochemistry Geophysics Geosystems*, *15*(12), 4958-4983.

Li, C.−F., Lin, J., Kulhanek, D. K., & the Expedition 349 Scientists (2015). Proceedings of the International Ocean Discovery Program, South China Sea Tectonics, (Vol. 349). College Station, TX: International Ocean Discovery Program. https://doi.org/10.14379/iodp.proc.349.2015

Li, J., Tang, S.H., Zhu, X.K., & Pan, C.X. (2017). Production and certification of the reference material GSB 04-3258-2015 as a 143Nd/144Nd isotope ratio reference. *Geostandards and Geoanalytical Research*, *41*, 255-262.

Li, Q.Y., Zhao, Q.H., Zhong, G.F., Jian, Z.M., Tian, J., Cheng, X.R., et al. (2007). Deepwater Ventilation and Stratification in the Neogene South China Sea. *Journal of China University of Geosciences*, *18*(2):98-108.

Li, X.H., Wei, G., Shao, L., Liu, Y., Liang, X., Jian, Z., et al. (2003). Geochemical and Nd isotopic variations in sediments of the South China Sea: a response to Cenozoic tectonism in SE Asia. *Earth and Planetary Science Letters*, *211*, 207-220.

Li, X. (2011). Mineralogical Genesis Investigation of Two Types of Cretaceous Oceanic Iron-Containing Sediments, (Doctoral dissertation). Nanjing: Nanjing University.

Liu, H. Q., Yumul, G. P., Jr, Dimalanta, C. B., Queaño, K., Xia, X. P., Peng, T. P., et al. (2020). Western Northern Luzon isotopic evidence of transition from proto south China Sea to South China Sea fossil ridge subduction. Tectonics, 39, e2019TC005639

Liu, H.Q., Yumul, G.P., Jr, Dimalanta, C.B., Queaño, K., Xia, X.P., Peng, T.P., et al. (2020). Western Northern Luzon isotopic evidence of transition from proto-South China Sea to South China Sea

fossil ridge subduction. *Tectonics*, *39*, e2019TC005639.

Liu, Z.F., Colin, C., Huang, W., Le, K.P., Tong, S.Q., Chen, Z., & Trentesaux, A. (2007). Climatic and tectonic controls on weathering in South China and the Indochina Peninsula: clay mineralogical and geochemical investigations from the Pearl, Red, and Mekong drainage basins. *Geochemistry Geophysics Geosystems*, *8*, Q05005.

Liu, Z. F., Colin, C., Li, X. J., Zhao, Y. L., Tuo, S. T., Chen, Z., et al. (2010). Clay mineral distribution in surface sediments of the northeastern South China Sea and surrounding fluvial drainage basins: source and transport. *Marine Geology*, *277*, 48-60.

Liu, Z.F., Zhao, Y., Colin, C., Stattegger, K., Wiesner, M.G., Huh, C., et al. (2016). Source-to-sink transport processes of fluvial sediments in the South China Sea. *Earth-Science Reviews*, *153*, 238-273.

Löwemark, L., Jakobsson, M., M¨orth, M., & Backman, J. (2008). Arctic Ocean manganese contents and sediment colour cycles. *Polar Research*, *27*(2), 105-113.

Lyle, M. (1983). The brown-green color transition in marine sediments: a marker of the Fe (III)-Fe (II) redox boundary. *Limnology and Oceanography*, *28*(5), 1026-1033.

Ma, X., Tian, J., Ma, W., Li, K., & Yu, J. (2018). Changes of deep Pacific overturning circulation and carbonate chemistry during middle Miocene East Antarctic ice sheet expansion. *Earth and Planetary Science Letters*, *484*, 253-263.

Mamet, B., & Préat, A. (2006). Iron-bacterial mediation in Phanerozoic red limestones: state of the art. *Sedimentary Geology*, *185* (3-4), 147-157.

Mevinier, A., Lanson, B., & Velde, B. (2004). Composition variation of illite-vermiculite-smectite mixed-layer minerals in a bentonite bed from Charente (France). *Clay Minerals*, *39*(3), 317-332.

McLennan, S.M. (1989). Rare earth elements in sedimentary rocks; influence of provenance and sedimentary processes. *Reviews in Mineralogy and Geochemistry*, *21*(1), 169-200.

Miller, K. G., Browning, J. V., Schmelz, W. J., Kopp, R. E., & Wright, J.D. (2020). Cenozoic sea-level and cryospheric evolution from deep-sea geochemical and continental margin records. *Science Advances*, *6*(20), eaaz1346.

Nesbitt H.W., & Young G.M. (1982). Early proterozoic climate and plate motions inferred from major element chemistry of lutites. *Nature*, *299*, 715-717.

Nesbitt, H.W., Fedo, C.M., & Young, G.M. (1997). Quartz and feldspar stability, steady and non-steady-state weathering, and petrogenesis of siliciclastic sands and muds. *Journal of Geology*, *105* (2), 173-191.

Paterson, G., & Heslop, D. (2015). New methods for unmixing sediment grain size data. *Geochemistry Geophysics Geosystems*, *16*, 4494-4506.

Qi, L., & Gregoire, D.C. (2000). Determination of trace elements in twenty six Chinese geochemistry reference materials by inductively coupled plasma-mass spectrometry. *Geostandards and Geoanalytical Research*, *24*(1), 51-63.

Schwertmann, U. (1971). Transformation of hematite to goethite in soils. *Nature*, *232*, 624-625.

Schwertmann, U. (1988). Occurrence and formation of iron oxides in various pedoenvironments. In Stucki, J.W., Goodman, B.A., Schwertmann, U. (Ed.), *Iron in soils and clayminerals* (pp. 267-308). Dordrecht: Springer.

Shao, L., Li, X., Geng, J., Pang, X., Lei, Y., Qiao, P., et al. (2007). Deep water bottom current deposition in the northern South China Sea. *Science in China Series D: Earth Sciences*, *50*, 1060-1066.

Song, H., Jiang, G., Poulton, S.W., Wignall, P.B., Tong, J., Song, H., et al. (2017). The onset of widespread marine red beds and the evolution of ferruginous oceans. *Nature Communications*, *8*, 399.

Stuut, J.-B.W., Prins, M.A., Schneider, R.R., Weltje, G.J., Jansen, J.H.F., & Postma, G. (2002). A 300-kyr record of aridity and wind strength in southwestern Africa: inferences from grain-size distributions of sediments on Walvis Ridge, SE Atlantic. *Marine Geology*, *180*, 221-233.

Sun, S.-S., & McDonough, W.F. (1989). Chemical and isotopic systematics of oceanic basalts: implications for mantle composition and processes. *Geological Society, London, Special Publications*, *42*, 313-345.

Talley, L.D. (2013). Closure of the global overturning circulation through the Indian, Pacific and Southern Oceans: Schematics and transports. *Oceanography*, *26*, 80–97.

Thirlwall, M. F. (1991). Long-term reproducibility of multicollector Sr and Nd isotope ratio analysis. *Chemical Geology*, *94*(2), 85-104.

Tribovillard, N., Algeo, T.J., Lyons, T., & Riboulleau, A. (2006). Trace metals as paleoredox and paleoproductivity proxies: An update. *Chemical Geology*, *232*, 12-32.

Wan, S.M., Li, A.C., Clift, P.D., & Stutt, J.B. (2007). Development of the East Asian monsoon: mineralogical and sedimentologic records in the northern South China Sea since 20 Ma. *Palaeogeography Palaeoclimatology Palaeoecology*, *254*, 561-582.

Wan, S.M., Kürschner, W.M., Clift, P.D., Li, A.C., & Li, T.G. (2009). Extreme weathering/erosion during the Miocene Climatic Optimum: evidence from sediment record in the South China Sea. *Geophysical Research Letters*, *36*, L19706.

Wan, S.M., Clift, P.D., Zhao, D.B., Hovius, N., Munhoven, G., France-Lanord, C., et al. (2017). Enhanced silicate weathering of tropical shelf sediments exposed during glacial lowstands: A sink for atmospheric CO_2. *Geochimica et Cosmochimica Acta*, *200*, 123-144.

Wang, C., Hu, X., Huang, Y., Scott, R., & Wagreich, M. (2009). Overview of Cretaceous oceanic red beds (CORB): a window on global oceanic and climatic change. In Hu, X., Wang, C., Scott, R.W., Wagreich, M., Jansa, L. (Eds.), *Cretaceous Oceanic Red Beds: Stratigraphy, Composition, Origins and Paleoceanographic and Paleoclimatic Significance* (Vol. 91, pp. 13-33). Tulsa, OK: Society for Sedimentary Geology Special Publication.

Wang, T.T. (2016). Fe isotope compositions of the Upper Cretaceous black shales and oceanic red beds and its implications to paleoceanography and paleoclimate, (Doctoral dissertation). Beijing: China University of Geosciences (Beijing).

Wedepohl, K. (1971). Environmental influences on the chemical composition of shales and clays. *Physics and Chemistry of the Earth*, *8*, 307-331.

Wignall, P. B., & Twitchett, R. J. (1996). Oceanic Anoxia and the End Permian Mass Extinction. *Science*, *272*, 1155-1158.

Wright, J.D., Miller, K.G., & Fairbanks, R.G. (1991). Evolution of modern deepwater circulation: evidence from the late Miocene Southern Ocean. *Paleoceanography*, *6*, 275-290.

Wright, J.D., & Miller, K.G. (1993). Southern Ocean Influences on Late Eocene to Miocene Deepwater Circulation. *Antarctic Research Series*, *60*, 1-25.

Zhang, W., Wei, X.Y., Zheng, J.H., Zhu, Y.L., & Zhang, Y.J. (2012). Estimating suspended sediment loads in the Pearl River Delta region using sediment rating curves. *Continental Shelf Research*, *38*, 35-46.

Zheng, X., Kao, S., Chen, Z., Menviel, L., Chen, H., Du, Y., et al. (2016). Deepwater circulation

variation in the South China Sea since the Last Glacial Maximum. *Geophysical Research Letters*, *43*(16): 8590-8599.

Ziegler, A., & McKerrow, W. (1975). Silurian marine red beds. *American Journal of Science*, *275*(1), 31-56.

Table 1. Iron geochemical data of marine red and green gray samples from U1503A and other regions

Area	Types of samples	Number of samples	Fe_2O_3 (%)	FeO (%)	Fe^{3+}/Fe^{2+}	Data source
IODP Site U1503A, SCS	Brown claystone	34	7.53	1.10	6.28	This study
	Green claystone	12	4.90	1.25	3.61	
Chuangde Section, Tibet	Red shale	14	8.39	1.77	4.27	Hu et al. (2006)
	Gray shale	2	1.77	6.68	0.24	
Chuangde Section, Tibet	Red limestone	4	4.27	1.80	2.14	Hu et al. (2006)
	Gray limestone	4	0.57	0.85	0.60	
Vispi Quarry Section, Italy	Red limestone	8	0.18	0.13	1.25	Li (2011)
	White limestone	5	0.08	0.11	0.65	
ODP Site 641A, Atlantic	Red mudstone	15	7.96	0.24	29.31	Wang (2016)
	Black shale	2	3.40	2.20	1.39	
Modern Pacific	Red clay		7.70	-	-	Glasby et al. (1991)

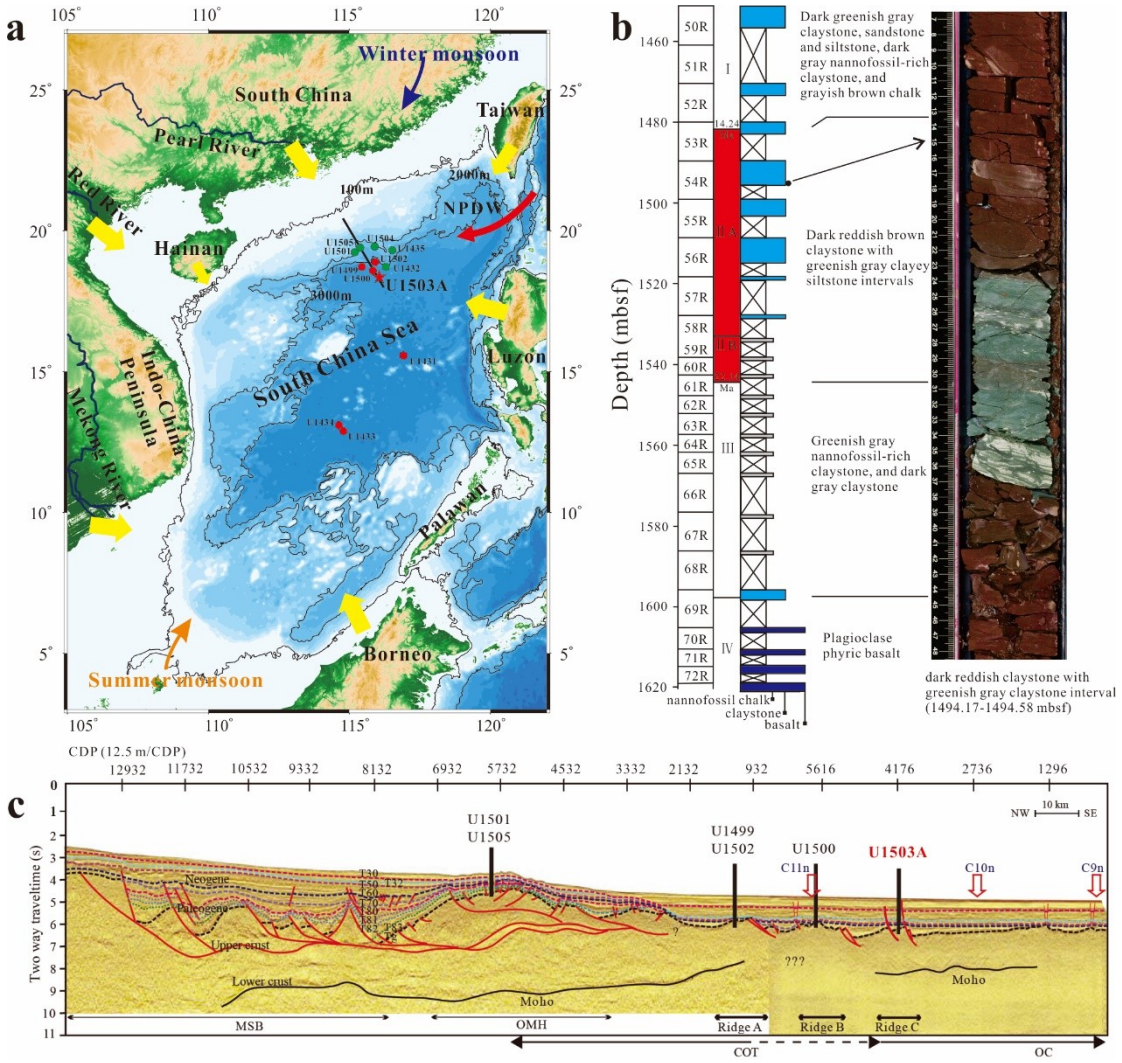
a
Winter monsoon
South China
Taiwan
Pearl River
Red River
Hainan
100m
2000m
NPDW
U1503A
3000m
South China Sea
Luzon
Indo-China Peninsula
Mekong River
Palawan
Borneo
Summer monsoon
b
Depth (mbsf)
Dark greenish gray claystone, sandstone and siltstone, dark gray nannofossil-rich claystone, and grayish brown chalk
Dark reddish brown claystone with greenish gray clayey siltstone intervals
Greenish gray nannofossil-rich claystone, and dark gray claystone
Plagioclase phyric basalt
dark reddish claystone with greenish gray claystone interval (1494.17-1494.58 mbsf)
nannofossil chalk
claystone
basalt
c
CDP (12.5 m/CDP)
Two way traveltime (s)
U1501
U1505
U1499
U1502
U1500
U1503A
C11n
C10n
C9n
NW
10 km
SE
Neogene
Paleogene
Upper crust
Lower crust
Moho
MSB
OMH
Ridge A
Ridge B
Ridge C
COT
OC

Fig.1. (a) Bathymetry map of South China Sea indicating the location of IODP sites in the South China Sea and the major river systems in East Asia. -100m, -2000m and -3000m isobaths are shown with gray lines. Thick black line is the position of the seismic line showing in Fig.1c. Red star indicates the location of Site U1503A. Red circles represent the other drill sites recovered brown claystone. Green circles are the drill sites without brown claystone. Modern summer and winter monsoons are shown by orange and dark blue arrows, respectively. NPDW = North Pacific Deep Water. Red arrow is the inflow of the NPDW. (b) Lithostratigraphy of Unit II of Site U1503A with selected core photo showing brown claystone with green gray claystone interbed. (c) Deep crustal time-migrated reflection seismic profile with interpretation. Site U1503A is located on the top of the basement high named Ridge C. MSB-Mid slope basin, OMH-Outer Margin High, COT-Continent Ocean Transition, OC-Oceanic crust, mbsf-meter below sea floor.

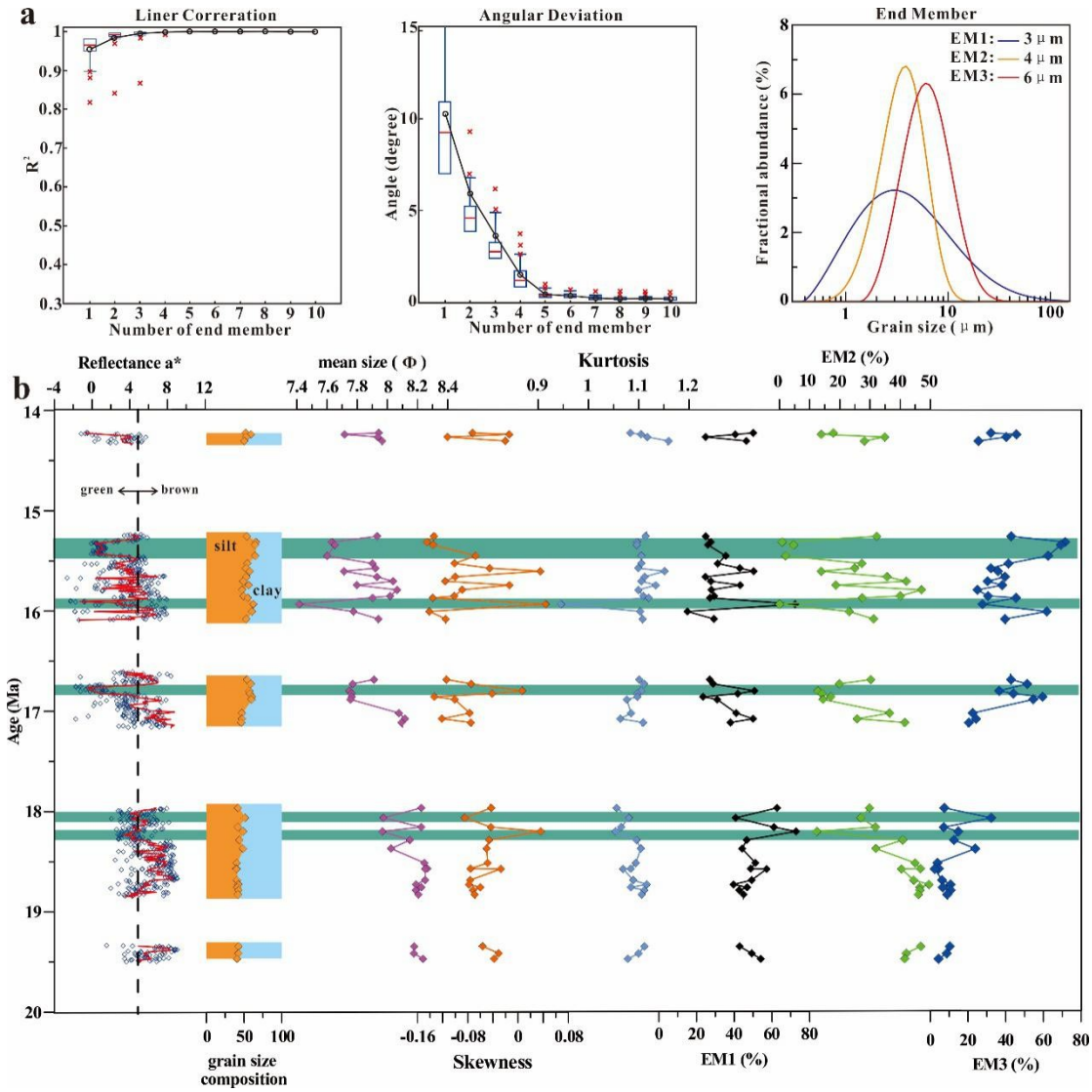

Fig.2. (a) End member modeling results of the terrigenous fraction in the sediments of Unit II. Three end members model is the best optimization (R^2>0.9, angular deviation<5). Grain size modes for EM1, EM2, and EM3 are 3μm, 4μm and 6μm, respectively. (b) Variations of grain size parameters (mean grain size, skewness, kurtosis, and sorting) and three end members. The shadow areas represent five thicker green claystone intervals. Red curve in reflectance a* is plotted with five-point running average, which is shown in the same way in the following figures.

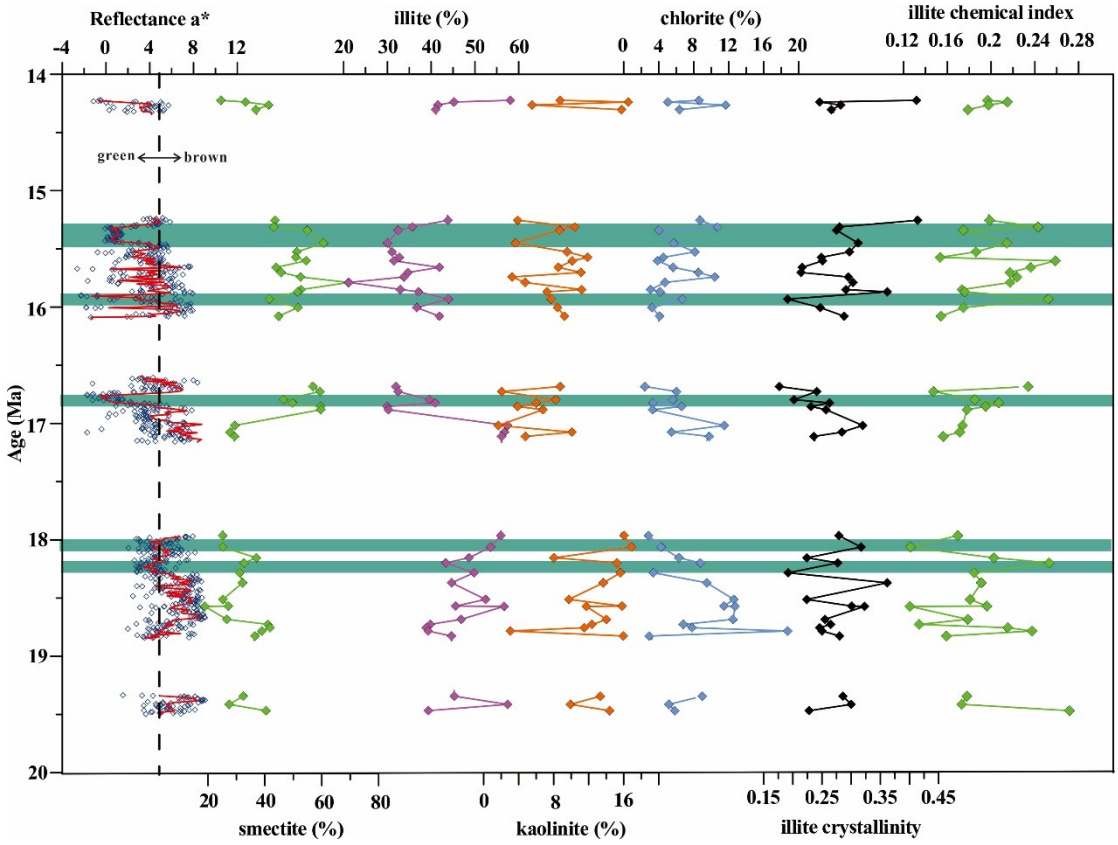

Fig.3. Variations in clay mineral assemblages (smectite, illite, kaolinite and chlorite percentages), illite crystallinity index and illite chemical index for Unit II. The shadow areas represent five thicker green claystone interbeds.

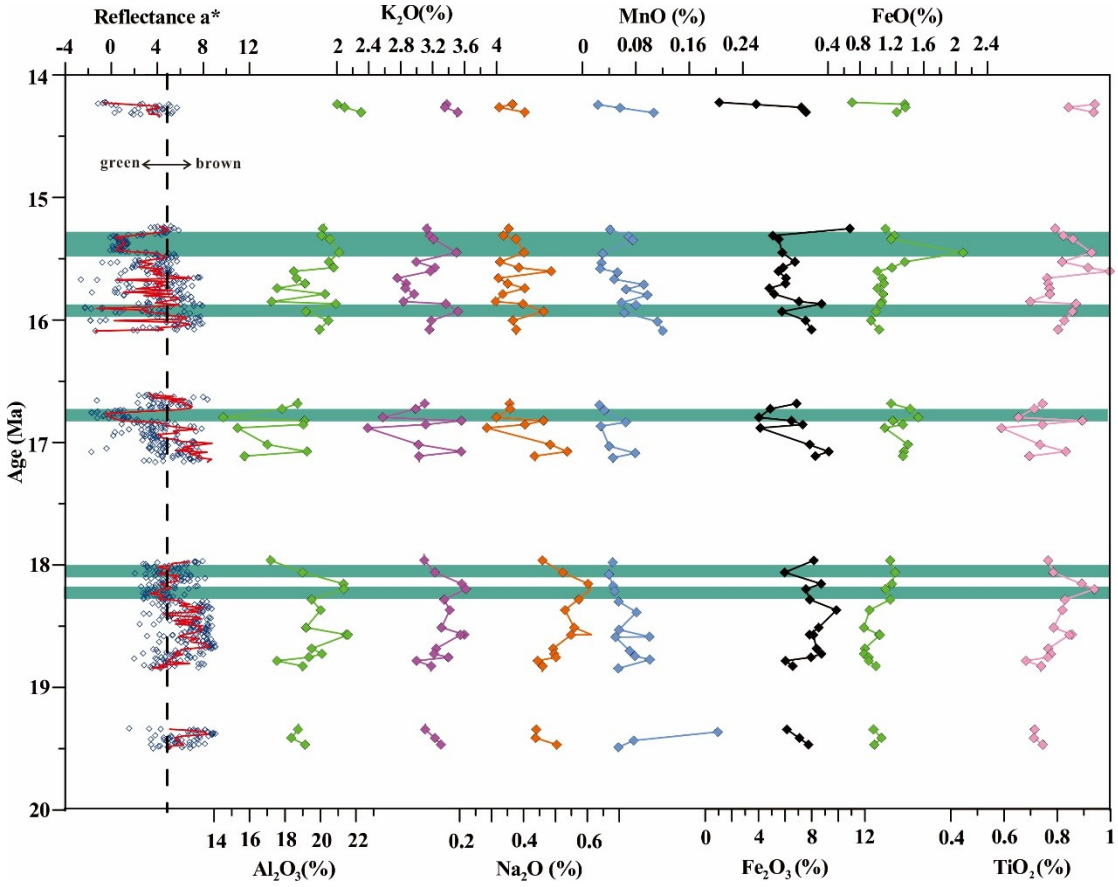

Fig.4. Variations of major element concentrations of Unit II samples from Site U1503A. The shadow areas represent the thicker green claystone interbeds.

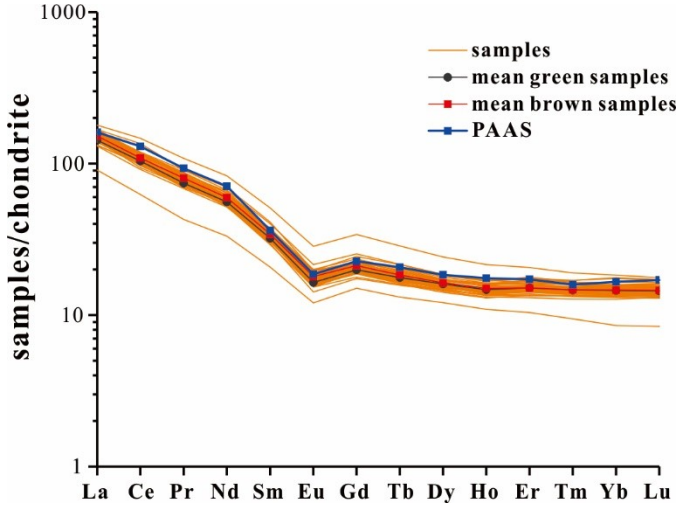

Fig.5. Chondrite normalized REE patterns of brown and green samples from Unit II of U1503A, as compared to the values of Post Archean Australian Shales (PAAS) (McLennan, 1989).

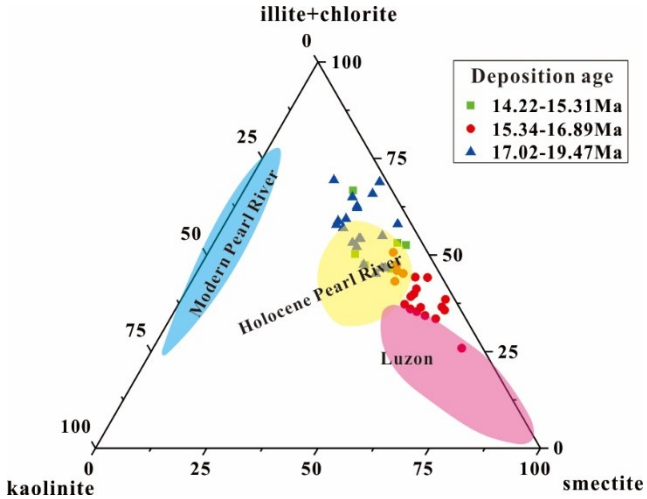

Fig.6. Ternary source discrimination diagram. It shows that the clay mineral composition of Unit II sediments from U1503A and their potential sources, including modern Pearl River, Holocene Pearl River (Hu et al., 2013), and Luzon (Liu et al., 2010).

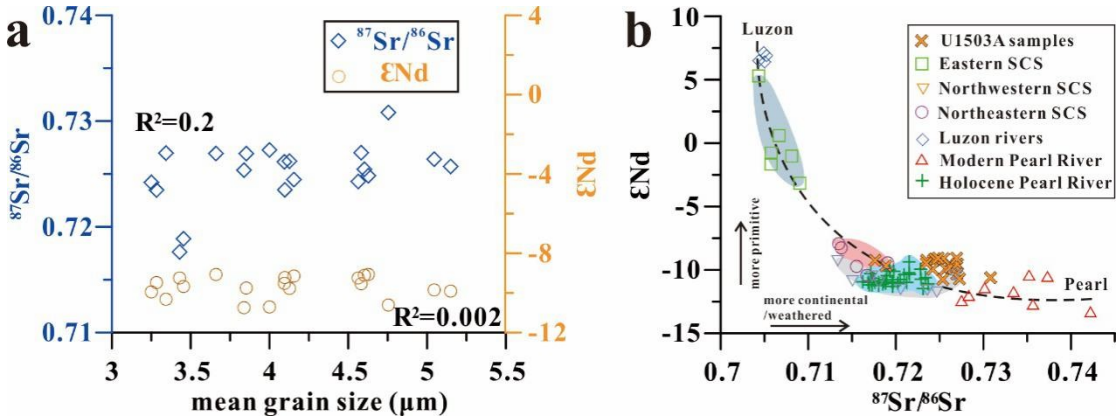

Fig.7. (a) Correlation analysis of grain size and Sr-Nd isotopes. There is no obvious correlation between grain size and Sr-Nd isotopes, suggesting insignificant grain size influence on Sr-Nd isotopes. (b) Sediment provenance discrimination diagram of Sr-Nd isotopes. For comparison, the Sr-Nd isotope data of sediments from Luzon rivers (Goldstein and Jacobsen, 1988), modern Pearl River (Liu et al., 2007), Holocene Pearl River (Hu et al., 2013) and SCS seafloor surface (Liu et al., 2016) are plotted. The dashed lines indicated two end-members mixing between Luzon and Pearl River.

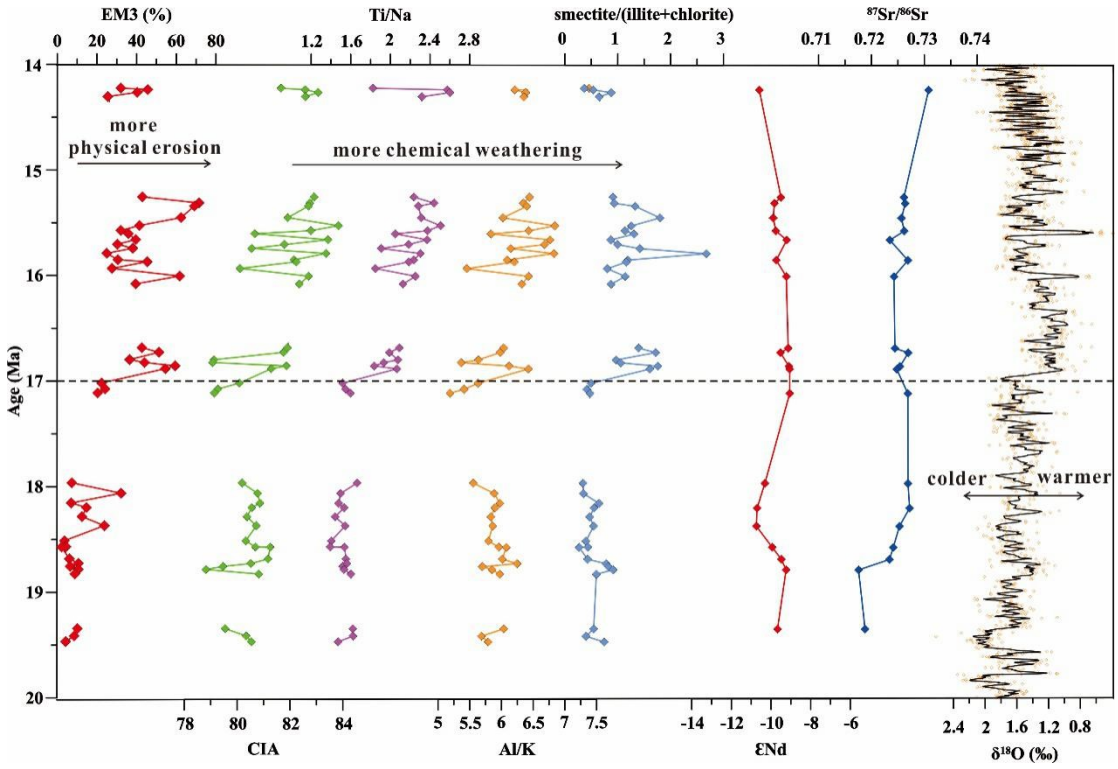

Fig.8. Variations of multiple weathering proxies (including EM3, CIA, Ti/Na, Al/K, and smectite/(illite + chlorite)), Sr-Nd isotopic composition and Pacific distributed benthic $\delta^{18}O$ records (Miller et al., 2020). Black curve in $\delta^{18}O$ plot is a five-point running average.

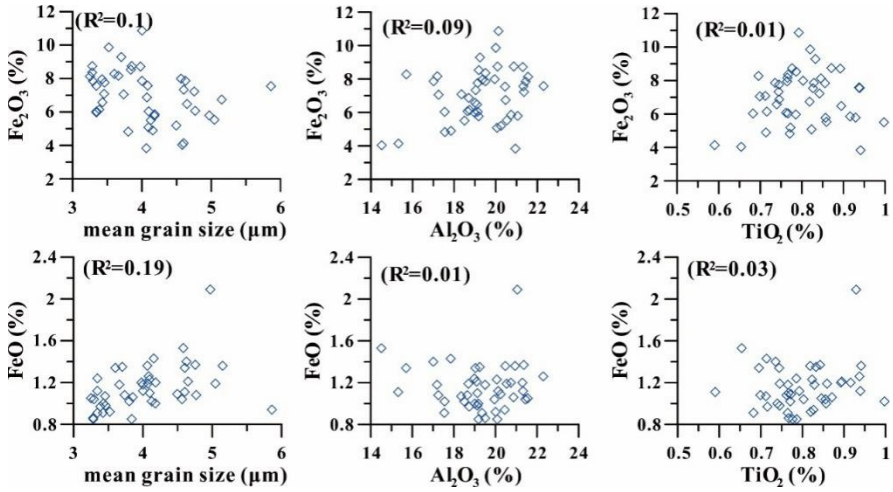

Fig.9. Correlation analysis of Fe_2O_3 and FeO with Al_2O_3, TiO_2 and grain size. Fe(II) and Fe(III) display poor correlation with terrigenous source elements (Al_2O_3 and TiO_2) and grain size, indicating great authigenic fraction influence on the Fe content.

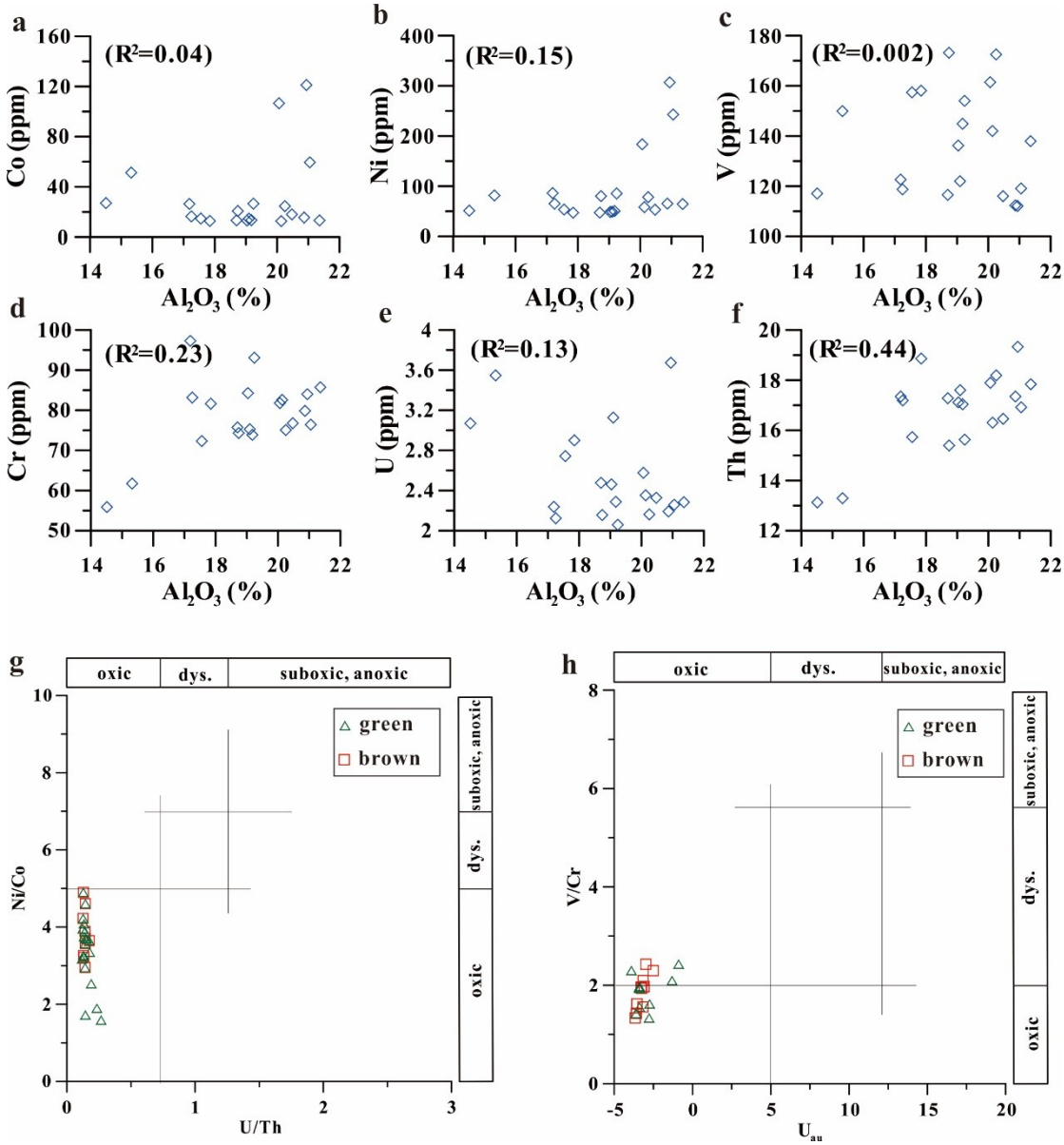

Fig.10. (a-f) Crossplots between Al_2O_3 and redox sensitive trace elements (Co, Ni, V, Cr, U, Th). Selected elements (except Th) show weak correlation with Al_2O_3, suggesting the significant authigenic fraction effect. (g-h) Redox environment discrimination diagram of redox sensitive trace elements ratios. Dys. = dysoxic. U_{au} (authigenic U) = total U-Th/3. The boundaries of oxic, dysoxic and anoxic environments are adopted from Jones and Manning (1994) and Wignall and

899Twitchett (1996).

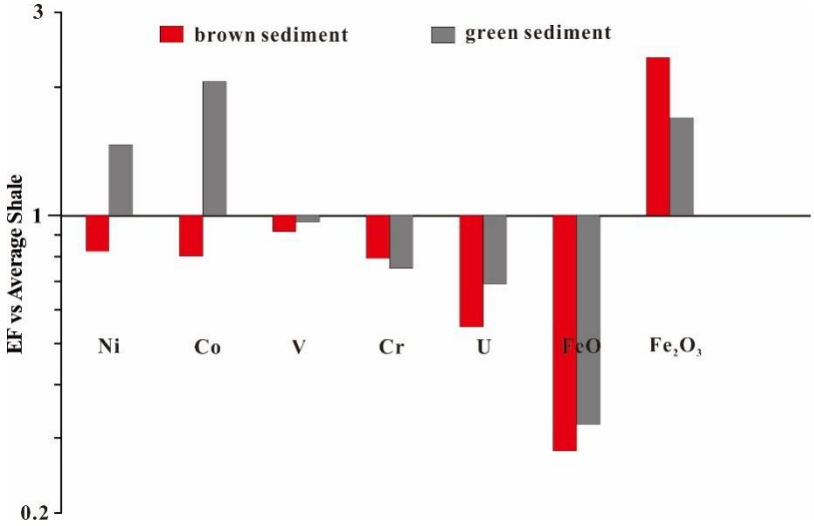

Fig.11 Enrichment factors (EF) relative to Average Shale (Wedepohl, 1971) for FeO, Fe_2O_3 and redox sensitive trace elements (Ni, Co, V, Cr, U).

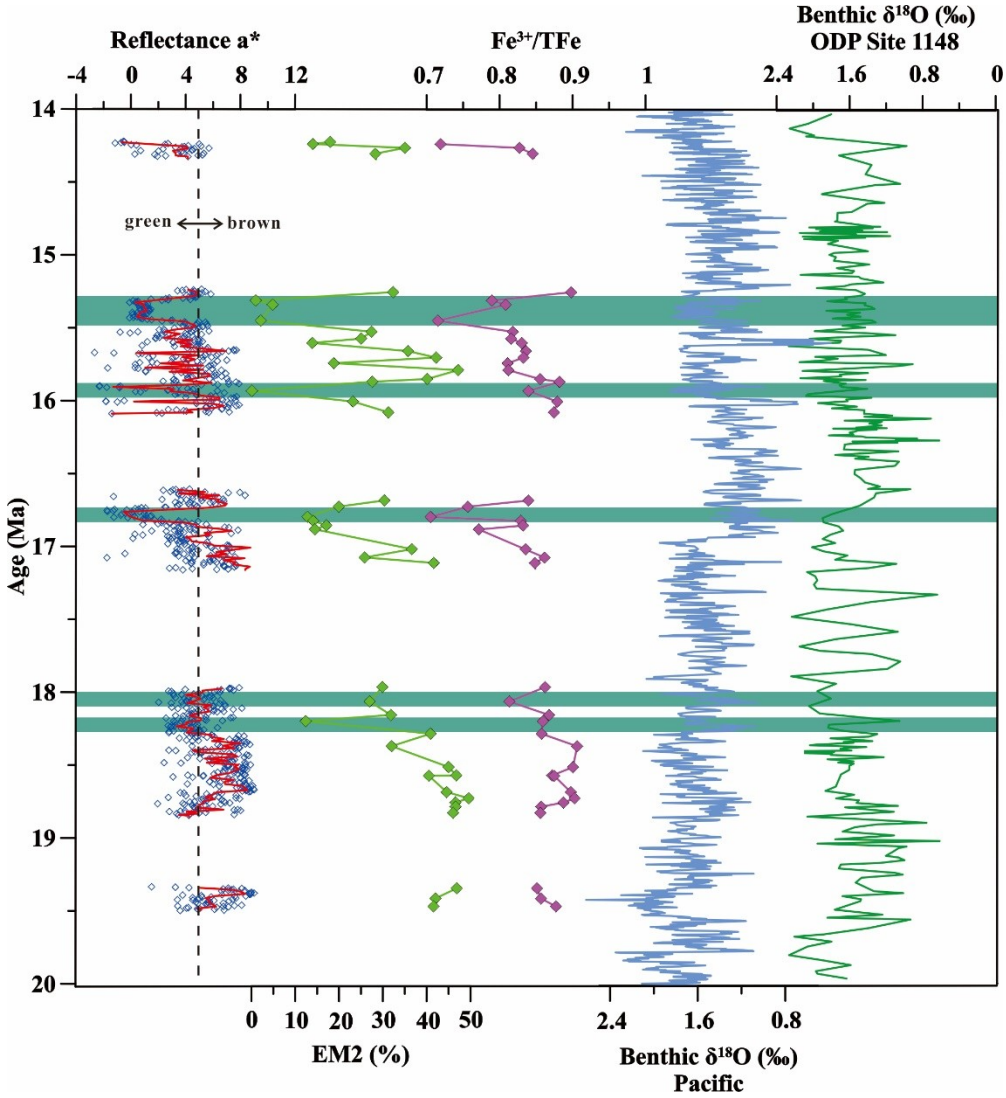

Fig.12 Variations of EM2, Fe^{3+}/TFe, ODP Site 1148 benthic $\delta^{18}O$ records (Cheng et al., 2004), and Pacific distributed benthic $\delta^{18}O$ records (Miller et al., 2020). The shadow areas represent the thicker green claystone interbeds.

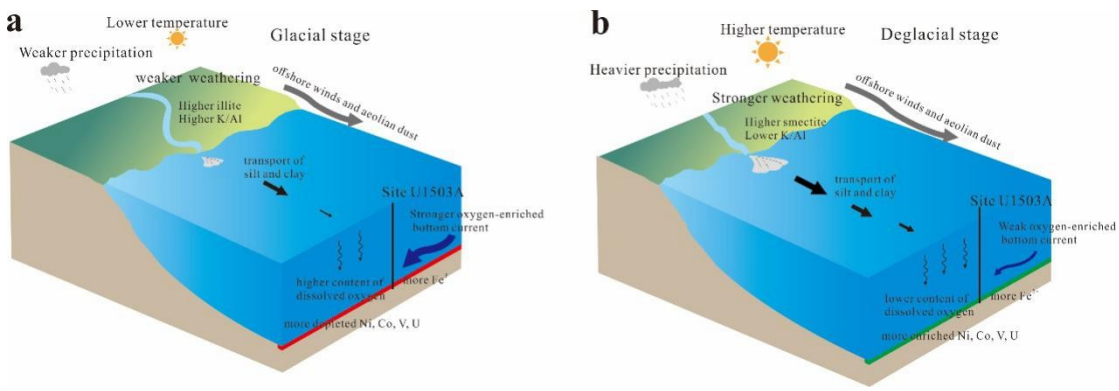

Fig.13 Conceptual models showing the paleoclimate and bottom current in relation to the Early-mid Miocene sediments in South China Sea. (a) Glacial stage with lower temperature, less humidity, stronger oxygen-enriched bottom current, contrasting with (b) deglacial stage with higher temperature, heavier rainfall and weaker oxygen-enriched bottom current.